

CTH-NT-320

THESIS FOR THE DEGREE OF DOCTOR OF PHILOSOPHY

# Control Rod Homogenization in Heterogeneous Sodium-Cooled Fast Reactors

MIKAEL ANDERSSON



Division of Subatomic and Plasma Physics  
Department of Physics  
S-412 96 Göteborg, Sweden 2016

Control Rod Homogenization in Heterogeneous Sodium-Cooled Fast Reactors  
MIKAEL ANDERSSON  
ISBN 978-91-7597-424-8

©Mikael Andersson, 2016

Doktorsavhandling vid Chalmers tekniska högskola  
Ny serie nr 4105  
ISSN 0346-718X

Division of Subatomic and Plasma Physics  
Department of Physics  
Chalmers University of Technology  
S-412 96 Göteborg  
Sweden  
Telephone +46 (0)31 772 1000

Cover: Spectral indicator showing spectral hardness at the follower/absorber interface in *3D*. Similar data is shown for a *2D* case in Fig. 5.1.

Chalmers Reproservice  
Göteborg, Sweden 2016

# Control Rod Homogenization in Heterogeneous Sodium-Cooled Fast Reactors

MIKAEL ANDERSSON

Division of Subatomic and Plasma Physics

Department of Physics

Chalmers University of Technology

## ABSTRACT

The sodium-cooled fast reactor is one of the candidates for a sustainable nuclear reactor system. In particular, the French ASTRID project employs an axially heterogeneous design, proposed in the so-called CFV (low sodium effect) core, to enhance the inherent safety features of the reactor.

This thesis focuses on the accurate modeling of the control rods, through the homogenization method. The control rods in a sodium-cooled fast reactor are used for reactivity compensation during the cycle, power shaping, and to shutdown the reactor. In previous control rod homogenization procedures, only a radial description of the geometry was implemented, hence the axially heterogeneous features of the CFV core could not be taken into account. This thesis investigates the different axial variations the control rod experiences in a CFV core, to determine the impact that these axial environments have on the control rod modeling.

The methodology used in this work is based on previous homogenization procedures, the so-called equivalence procedure. The procedure was newly implemented in the PARIS code system in order to be able to use 3D geometries, and thereby be able to take axial effects into account.

The thesis is divided into three parts. The first part investigates the impact of different neutron spectra on the homogeneous control-rod cross sections. The second part investigates the cases where the traditional radial control-rod homogenization procedure is no longer applicable in the CFV core, which was found to be 5-10 cm away from any material interface.

In the third part, based on the results from the second part, a 3D model of the control rod is used to calculate homogenized control-rod cross sections. In a full core model, a study is made to investigate the impact these axial effects have on control rod-related core parameters, such as the control rod worth, the capture rates in the control rod, and the power in the adjacent fuel assemblies. All results were compared to a Monte Carlo-based model which served as the reference.

It was demonstrated that the treatment of the radial environment, surrounding the control rod, has a small impact on the core parameters, and the traditional radial homogenization procedure yields reliable results. For axial interfaces within the control rod itself, the traditional radial homogenization procedure could no longer capture the large environmental impact, hence 3D modeling is recommended.

*Keywords:* Control rod, Homogenization, Fast Reactors, Reactivity Equivalence, Monte Carlo



## Preface

As a part of the negotiations in 2010, regarding the European Spallation Source (ESS) which is being built in the south of Sweden, a large research agreement was signed between Sweden and France. This research agreement was outlined as a collaboration, where Sweden would send a number of PhD students and postdoctoral fellows to France to work with French projects. The topic for this collaboration was decided to be nuclear energy, divided into projects regarding the prototype reactor ASTRID and the Jules Horowitz reactor. The collaboration was funded by the Swedish Research Council.

This thesis is part of the joint project *Core physics, diagnostics, and instrumentation for enhanced safety of the sodium-cooled fast reactor ASTRID*, and is outlined as a collaboration between Chalmers University of Technology, Sweden, and CEA Cadarache, France. During this project, which spanned over four years, I spent 2.5 years at the CEA Cadarache site in the south of France (where my office had a nice view over the Jules Horowitz reactor, that was under construction). The first year and the last six months of the project I spent at my university, Chalmers.

My hopes are that the outcome of this project will be of use for the continuation of the ASTRID project and other fast reactor projects.

Mikael Andersson  
Göteborg 2016/05/30



## Appended papers

This thesis is an introduction to and a summary of the work published in the following papers

### PAPER I

M. Andersson, D. Blanchet, H. Nylén, and R. Jacqmin. "Influence of Local Spectral Variations on Control-Rod Homogenization in Fast Reactor Environments". In: *Nucl. Sci. Eng* 181.2 (2015), pp. 204–215

*The first author performed all simulations, the main part of the analysis and wrote the manuscript. The second author was involved in the analysis and the technical aspects of the manuscript. The third and fourth authors were involved in the outline and the proof reading of the manuscript.*

### PAPER II

M. Andersson, D. Blanchet, H. Nylén, and R. Jacqmin. "Control Rod Calculation in Axially-Heterogeneous Fast Reactors. Part I: Influence of the Absorber Environment". In: *Nucl. Sci. Eng* (In Press)

*The first author performed all simulations, the programming needed, the main part of the analysis and wrote the manuscript. The second author was involved in the analysis and the technical aspects of the manuscript. The third and fourth authors were involved in the outline and the proof reading of the manuscript.*

### PAPER III

M. Andersson, D. Blanchet, H. Nylén, and R. Jacqmin. "Control Rod Calculation in Axially-Heterogeneous Fast Reactors. Part II: Impact of 3D Homogenization on Core Parameters". In: *Nucl. Sci. Eng* (In Press)

*The first author performed all simulations, the programming needed, the main part of the analysis and wrote the manuscript. The second author was involved in the analysis and the technical aspects of the manuscript. The third and fourth authors were involved in the outline and the proof reading of the manuscript.*

### PAPER IV

M. Andersson, D. Blanchet, H. Nylén, and R. Jacqmin. "Impact of Control Rod Position and Homogenization on Sodium Void Effect in CFV-type SFR". in: *PHYSOR*, (Peer-reviewed). Idaho Falls, USA: American Nuclear Society, May 2016

*The first author performed all simulations, the programming needed, the main part of the analysis and wrote the manuscript. The second author was involved in the analysis and the technical aspects of the manuscript. The third and fourth authors were involved in the outline and the proof reading of the manuscript.*



### **Related work not included in this thesis**

M. Andersson, D. Blanchet, H. Nylén, and R. Jacqmin. “Influence of Local Spectral Variations on Control-Rod Homogenization”. In: *International Youth Nuclear Congress, (Abstract)*. Burgos, Spain: IYNC, July 2014

M. Andersson. “Control Rod Modeling in Axial Heterogeneous Fast Sodium Cooled Reactors”. In: *The 17th Meeting on Reactor Physics in the Nordic Countries, (Abstract)*. Gothenburg, Sweden: Chalmers, May 2015

M. Andersson, D. Blanchet, H. Nylén, and R. Jacqmin. “Impact of 3D Modeling and Homogenization of Control Rod on Reactivity in CFV-type SFR Cores”. In: *ANS winter meeting, (Peer-reviewed)*. Washington DC, USA: American Nuclear Society, Nov. 2015



<b>Abstract</b>	<b>I</b>
<b>Preface</b>	<b>III</b>
<b>List of publications</b>	<b>V</b>
<b>Abbreviations &amp; Nomenclature</b>	<b>XI</b>
<b>1 Introduction</b>	<b>1</b>
1.1 Objective . . . . .	1
1.2 Outline . . . . .	2
<b>2 Background</b>	<b>5</b>
2.1 Sustainable Nuclear Power & Nuclear waste . . . . .	5
2.1.1 Generation IV . . . . .	6
2.2 Sodium Cooled Fast Reactors . . . . .	7
2.2.1 The CFV Core . . . . .	9
2.3 Reactivity Control Systems for Fast Reactors . . . . .	10
2.3.1 The Control Rod Systems in the CFV core . . . . .	12
<b>3 Methodology</b>	<b>13</b>
3.1 Neutron Calculations . . . . .	13
3.1.1 Homogenization Methods . . . . .	14
3.2 Computational Tools . . . . .	15
3.2.1 ERANOS 2 . . . . .	15
3.2.2 PARIS . . . . .	16
3.2.3 TRIPOLI-4 <sup>®</sup> . . . . .	16
3.3 Homogenization with Reactivity Equivalence . . . . .	16
3.3.1 Derivation of the Equivalence Procedure . . . . .	16
3.4 Implementation . . . . .	21
3.4.1 Numerical Stability Enhancement . . . . .	23
3.5 The Classical Equivalence Procedure . . . . .	25
<b>4 Spectral Impact on Cross Sections</b>	<b>27</b>
4.1 Spectral Shifts . . . . .	27
4.2 Impact of Resonances . . . . .	29

4.3	Impact of Spectral Softening . . . . .	31
<b>5</b>	<b>Characterization of Axial Regions</b>	<b>33</b>
5.1	Control Rod Environments . . . . .	33
5.2	Means of Characterization . . . . .	35
5.3	Interface Characteristics . . . . .	36
5.3.1	Absorber/Follower Interface . . . . .	36
5.3.2	Core Environments . . . . .	37
5.4	Remarks . . . . .	39
<b>6</b>	<b>Impact on Core Parameters</b>	<b>41</b>
6.1	Control Rod Related Parameters . . . . .	41
6.2	Control Rod Partitioning . . . . .	42
6.2.1	Control Rod Homogenization . . . . .	43
6.3	Calculation Route . . . . .	44
6.3.1	The TRIPOLI-4 <sup>®</sup> Reference Model . . . . .	45
6.4	Reactivity Effects . . . . .	45
6.4.1	Reactivity Effect of Individual Environments . . . . .	47
6.4.2	Fine Partitioning of the Follower/Absorber Interface . . . . .	48
6.4.3	Sodium Void Reactivity Effect . . . . .	48
6.5	Impact on Reaction Rate . . . . .	49
<b>7</b>	<b>Summary and Future Work</b>	<b>51</b>
7.1	Summary . . . . .	51
7.1.1	Impact of Environmental Differences . . . . .	51
7.1.2	Disadvantages & Complications . . . . .	52
7.2	Conclusions . . . . .	53
7.3	Outlook . . . . .	53
	<b>Acknowledgements</b>	<b>55</b>
	<b>References</b>	<b>56</b>
	<b>Papers I-IV</b>	<b>61</b>

### Abbreviations

<b>B<sub>4</sub>C</b>	Boron carbide
<b>BOC</b>	Beginning of cycle
<b>BOL</b>	Beginning of life
<b>CEA</b>	Commissariat à l'Énergie Atomique et aux Énergies Alternatives
<b>CFV</b>	<i>Cœur à Faible effet de Vide sodium; Low sodium void effect core</i>
<b>CRW</b>	Control rod worth
<b>CSD</b>	Control shutdown system
<b>DSD</b>	Diverse shutdown system
<b>ECXS</b>	Environmentally corrected equivalent cross sections
<b>EOC</b>	End of cycle
<b>LWR</b>	Light water reactor
<b>MOX</b>	Mixed oxide
<b>pcm</b>	10 <sup>-5</sup> (= per cent mill)
<b>P<sub>N</sub></b>	Spherical harmonics of order <i>N</i>
<b>SFR</b>	Sodium-cooled fast reactor
<b>S<sub>N</sub></b>	Discrete ordinate of order <i>N</i>
<b>SP<sub>N</sub></b>	Simplified spherical harmonics of order <i>N</i>
<b>SVRE</b>	Sodium void reactivity effect
<b>T4</b>	TRIPOLI-4®
<b>TEXS</b>	Traditional equivalent cross sections
<b>UOX</b>	Uranium oxide

## Nomenclature

$\psi$	angular flux
$\phi$	scalar flux
$\psi^\dagger$	adjoint angular flux
$\Sigma$	macroscopic cross section
$\sigma$	microscopic cross section
$\vec{r}$	spatial variable
$E$ or $g$	energy variable (continuous or group structure)
$\Omega$	angular direction
$k$	effective multiplication factor
$\rho$	reactivity $\frac{k-1}{k}$
$\nu$	mean number of emitted neutrons per fission
$\beta$	delayed neutron fraction
$\bar{\sigma}_x^i$	spectral indicator
$R_x$	reaction rate

# CHAPTER 1

## Introduction

*This chapter introduces the topic and the project, as well as the limitations, and the outline of this thesis.*

### 1.1 Objective

Since the early 1940s, when the nuclear era began with the Manhattan project and *Chicago Pile-1* [1], the first man-made critical system, a number of different reactor concepts have been designed and some of them built. During the early years, two reactor types were considered: the fast reactor, and the thermal reactor. The first reactor built providing electricity was the fast reactor *EBR-1* [2] (lighting four 200 W light bulbs). However, for the commercialization of nuclear power plants, the thermal Light Water Reactors (LWRs) took the lead because of the simpler designs and the fact that no new technology was needed for steam based electricity production. At present, the majority of the nuclear power plants under operation are of LWR type, and are of the second generation of nuclear power plants (Gen-II). One disadvantage with thermal reactors using uranium-based fuel is the poor fuel utilization, where large amount of radioactive waste will be produced, containing a large amount of uranium combined with most of the elements and isotopes of the periodic table. With a fast reactor on the other hand, the fuel utilization can be increased and with an appropriate design, reprocessed spent fuel (the waste) from LWRs can be used as fuel for fast reactors.

All the nuclear plants presently under construction are LWRs of the third generation (Gen-III or Gen-III+). Gen-III reactors are thermal reactors using the same concepts as Gen-II, however with enhanced safety systems, relying more on natural laws, and more redundancy in the active systems to ensure a safe operation, and to minimize the likelihood and fallout of a severe accident. The fourth generation of nuclear power (Gen-IV) is a research initiative [3] aimed at investigating a new concept of nuclear reactors, different from the Gen-II and Gen-III concepts. Within Gen-IV, six different reactor concepts are investigated, both of thermal and fast reactor designs, but with the common goals of: sustainability, economics, safety, and proliferation resistance.

One of the reactor concepts investigated in the Gen-IV initiative is the Sodium-

cooled Fast Reactor (SFR), which is a fast reactor concept with liquid sodium as a coolant (instead of water as in LWRs). The SFR is not a new concept; over the years a number of test reactors were built based on this concept, including *EBR-II* in the US [4], *Phénix* [5] and *Superphénix* [6] in France, *BN-600* [7] and *BN-800* [8] in Russia, and *Monju* [9] in Japan. One of the main projects concerning SFRs today, is the Advanced Sodium Technological Reactor for Industrial Demonstration (ASTRID) project in France, with the CFV core concept [10] (French acronym of *Cœur à Faible effet de Vide sodium*, meaning *low sodium void effect core*).

Since one of the goals with Gen-IV reactors is enhanced safety, reliable modeling tools are required to be able to predict the behavior of the reactor during operation and during postulated accident scenarios. For the safety assessment of a reactor, a number of different safety margins have to be considered, such as the Control Rod Worth (CRW), and the shut down margin of the reactor. In a SFR, the control rods are the only means of reactivity control, shutting the reactor down, and power shaping, hence a reliable modeling of the control rods is essential. A correct prediction of the reactivity effect of the control rods in fast reactor systems was found to be problematic already during the seventies [11], and during the *Superphénix* start-up tests [12] large discrepancies were found between the calculated CRW and the measured data, hence new modeling procedures were needed.

The research presented in this thesis focuses on deterministic control rod modeling in a CFV-type core. The objective is to: investigate how the axial heterogeneities in the CFV-core affects the control rod, fulfill the required accuracy for the CRW modeling, as well as highlight the limitations of the modeling and the present control rod homogenization procedures. This project focuses on the calculation methods regarding control rod homogenization, not the design work, hence no design options are investigated and pre-conceptual designs of SFRs are used throughout the work. However, some of the general conclusions are expected to remain valid for other fast reactor concepts with similar control rod designs.

## 1.2 Outline

The first three chapters of this thesis give an introduction to the topic, the SFR, the CFV core concept, the SFR control rods, and the computational tools and methodologies used for control rod modeling and core calculations.

Chapters 4-6 summarize the appended papers, which concern models with increasing order of spatial dimensions. Chapter 4 covers Paper I, in which a simple *1D* model is used to study the impact the shifts in the neutron energy spectrum have on the control rod modeling. Chapter 5 covers Paper II, where different *2D* models were used to identify spectral regions in the CFV core, where the traditional homogenization procedures can be questioned and special treatment of the control rod might be necessary. Chapter 6 covers Papers III-IV, where the control rod absorber is homogenized by utilizing a *3D* model in order to assess

the impact the different axial regions identified in Paper II have on the main control-rod related core parameters in a CFV core.



## CHAPTER 2

## Background

*This chapter introduces the fast reactor systems and the Sodium-cooled Fast Reactor. The chapter finishes with an introduction of the typical control rod in fast reactors which is the main topic of this thesis.*

### 2.1 Sustainable Nuclear Power & Nuclear waste

Most countries that have a fleet of nuclear power plants, use the so called once-through fuel cycle [13], which means that the fuel is used once in the reactor, and is afterwards considered as nuclear waste. With the once through fuel cycle the waste has to be taken care of for about 100 000 years, before the radiation levels are at the same level as the background radiation from uranium ore. One of the candidates for such a storage is the deep geological depository developed in Sweden and Finland [14], with Finland being the first country to build one [15].

A typical spent fuel from a PWR consists of 95.5% uranium (1% U-235), 1% plutonium and higher actinides, and 3.5% fission products [13]. The radiotoxicity for the different parts of the spent fuel is shown in Fig. 2.1, where it can be seen that the main contributors to the long storage need are plutonium and americium, followed by curium and neptunium.

Some countries, like France, uses the fuel twice in some reactors. After discharge, the fuel is reprocessed, where the fission products, uranium, plutonium, and americium are separated. The uranium and plutonium are used once again in a reactor as Mixed Oxide Fuel (MOX). However, this can only be done once, since the isotopic content of the plutonium will change, and no longer be suitable for a thermal LWR [13].

To be able to utilize the uranium and plutonium fully, a different reactor type than a LWR is needed, for instance a fast reactor combined with a reprocessing facility. By using a fast spectrum and utilizing the plutonium, the fuel can be used much more efficiently, leaving a waste solely composed of fission products, and the required time in the depositories is reduced to 500-1000 years, as seen in Fig. 2.1. One of the reasons why a fast spectrum is better suited for plutonium-based fuel (compared with fuel based on U-235 as the fissile isotope), is that the plutonium

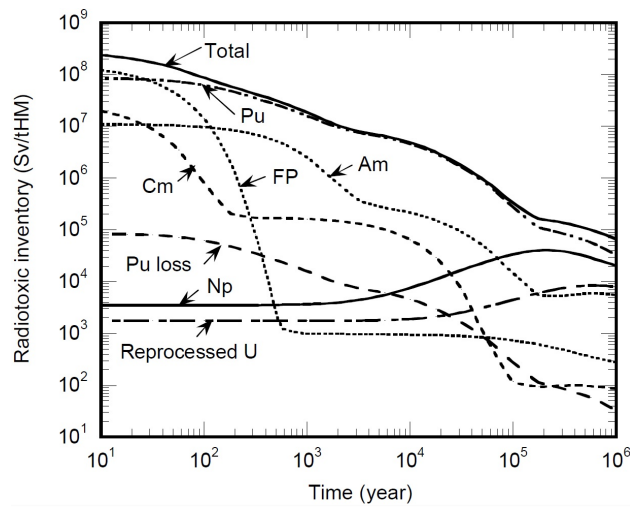


**Figure 2.1:** Radiotoxicity level for different actinides and fission products for a PWR fuel bundle [16]. Where the reprocessed U represents pure uranium, and Pu loss the amount of Pu left in the uranium after the separation process.

has a higher fission cross section in the higher energy range. The higher fission cross section combined with a lower capture cross section at high energies grants a better fission/absorption ratio for plutonium in a fast spectrum than for a thermal spectrum [13]. An example of this can be seen in Fig. 2.2, where the fission and capture cross sections are shown for Pu-239.

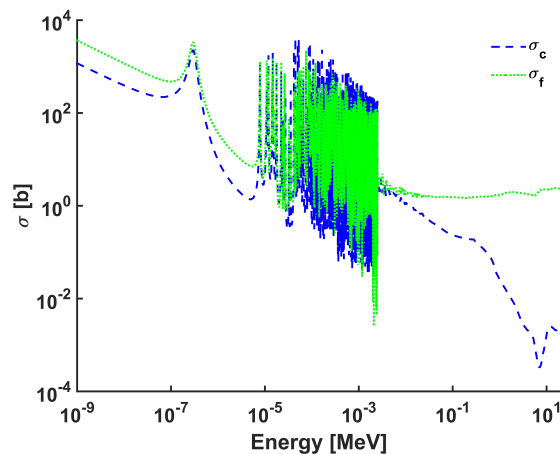


**Figure 2.2:** Fission and capture cross section for Pu-239 [17].

### 2.1.1 Generation IV

The Generation IV International Forum (GIF) was launched in 2000 and consists of 13 countries [3]. In 2002, a roadmap was created for the R&D of the new generation of nuclear reactors. The GIF roadmap has four main goals: sustainability, safety

and reliability, economic competitiveness, and proliferation resistance and physical protection. To focus the world effort within GIF, six different reactor types were chosen, both thermal and fast systems:

- Sodium cooled fast reactor (fast)
- Lead cooled fast reactor (fast)
- Gas cooled fast reactor (fast)
- Molten salt reactor (fast/thermal)
- Very high temperature reactor (thermal)
- Supercritical water-cooled reactor (fast/thermal)

Throughout this thesis, the only reactor concept studied is the SFR. However, for the fast reactor concepts (sodium, gas, and lead cooled) similar designs are utilized, except for the choice of coolant [18, 19, 20].

## 2.2 Sodium Cooled Fast Reactors

The SFRs use liquid sodium as a coolant, compared with LWRs that use water. By using sodium as a coolant a fast neutron flux is achievable, since sodium is a heavier atom compared with both oxygen and hydrogen that can be found in the coolant of LWRs, hence neutrons lose less energy in each scattering event. Even though sodium is a poor moderator, it will slightly soften the neutron spectrum. In the case of some accident scenarios where the heat removal is compromised, the sodium can start to boil. Hence, the softening effect of sodium is removed and comparatively, the neutron spectrum will harden in the fuel. Since the fission cross section in plutonium (and uranium) as well as the mean number of emitted neutrons in each fission ( $\nu$ ) is higher for higher energies, the reactivity will increase in such voided situations [21]. This effect is called the sodium void reactivity effect (SVRE).

Sodium has a high thermal conductivity and a large temperature span between solid state and vaporization (melting temperature of 371 K and boiling temperature of 1156 K). When used as a coolant, the core does not have to be pressurized, yet having a large margin to boiling. Due to the high thermal conductivity, a higher fuel/coolant ratio is attainable. To achieve a higher fuel/coolant ratio, a hexagonal lattice is used for the fuel pins, instead of the square lattice most commonly used for LWRs. An example of such a fuel subassembly from the *SuperPhénix* reactor can be seen in Fig. 2.3. The MOX pellets are encased in a stainless steel cladding, spaced with a wrapper wire to prevent flow blockage. Stainless steel is not used as the cladding material in thermal reactor systems like LWRs, because of the relatively high absorption cross section for Fe-56 (main isotope in steel) at thermal

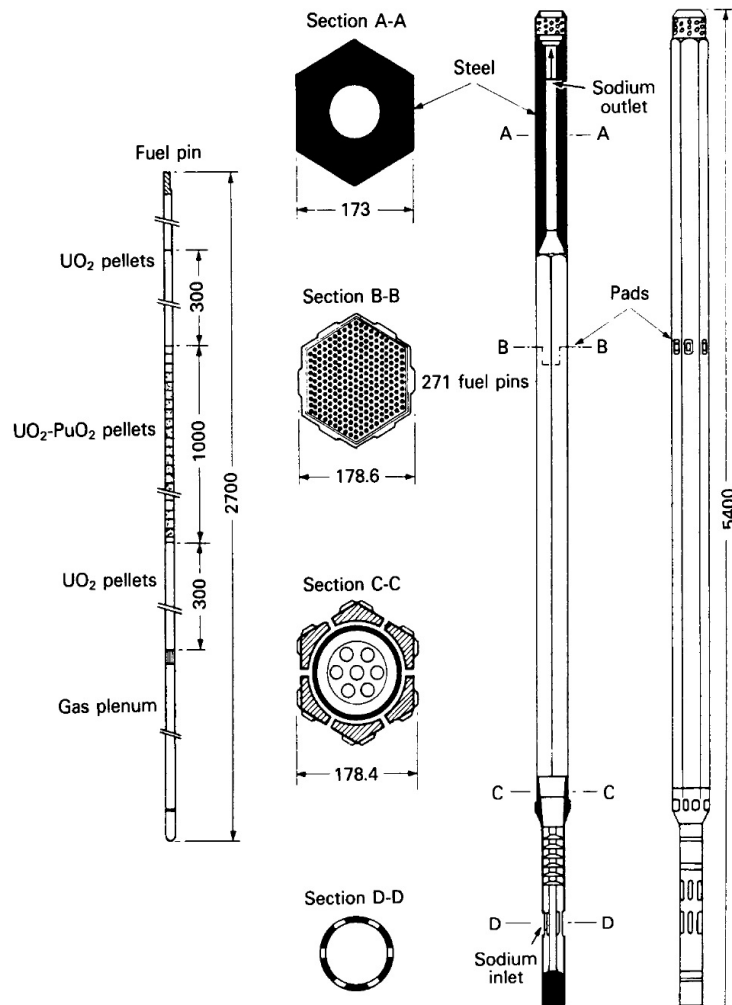


Figure 2.3: Fuel subassembly design for the *SuperPhénix* reactor [6].

energies. However, in a fast neutron spectrum this is no longer the case, and stainless steel is a suitable material for the cladding.

Sodium as a material is a chemically reactive substance in contact with water, therefore extra precautions have to be taken to ensure that no contact between sodium and water is possible. Especially when designing the heat exchanger and with fuel handling when it is removed from the core.

In general, the SFR cores are pancake-shaped with a small fuel height (around 1 m). This construction allows for an increased neutron leakage to compensate and reduce the voiding effect of sodium. In some core designs, the leaked neutrons are used for plutonium breeding by introducing a fertile blanket. To increase the power of a SFR, the number of fuel subassemblies is increased, expanding the core radially, not axially. Examples of this are the *Phénix* reactor (350 MW), with a core height of 85 cm and 102 fuel subassemblies [5], and the *SuperPhénix* (3000 MW), with a core height of 100 cm and 364 fuel subassemblies [6].

### 2.2.1 The CFV Core

The CFV core [10] is a French innovative SFR, that has been designed to fulfill the requirements of the Gen IV initiative [3]. The CFV core model used in this thesis (Chapters 5-6) is based on a pre-conceptual design of the ASTRID core [22]. The radial and axial map can be seen in Fig. 2.4, and the main design parameters can be found in Tab. 2.1. As can be seen in Fig. 2.4, the inner fuel subassemblies are axially heterogeneous with two fissile zones, sandwiching a fertile blanket. The outer fuel subassemblies only have one fissile region, and are 10 cm higher than the inner fuel zone, to increase the radial neutron leakage. Above the active core (inner and outer fuel zones), a sodium plenum and an upper neutron shield are situated. Below the active core a fertile blanket is situated for plutonium breeding.

The core model used in this work is a 1500 MW (thermal) SFR, where the active core consists of 291 fuel subassemblies (177 in the inner region and 114 in the outer region), radially surrounded by a stainless steel reflector. Each fuel subassembly consists of 271 pins, built up by MOX pellets in a stainless steel cladding. For non-proliferation purposes, the breeding gain is designed to be close to zero (only breeding enough plutonium to be self sustaining). In addition, no pure fertile subassemblies are present in the radial blanket to avoid subassemblies with easily accessible plutonium. The fertile pellets consist of either depleted or natural uranium oxide (UOX).

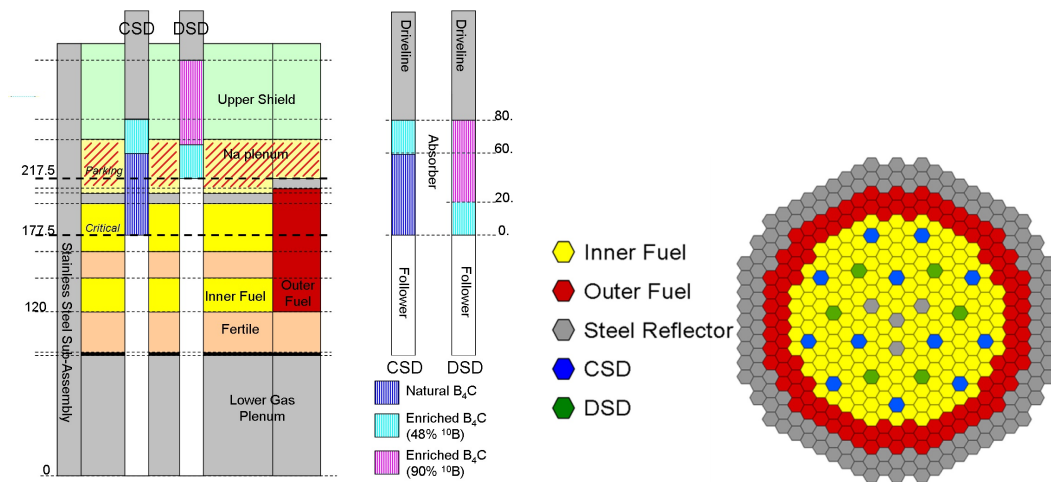


**Figure 2.4:** The axial core model (left figure), the axial geometry of the control rods (middle figure), and the radial core model (right figure). The figure is obtained from [23], but it is modified for this thesis.

In previous SRF designs, the SVRE was positive [10]. To increase the inherent safety features in the CFV-core, the axially heterogeneous design was proposed (see Fig. 2.4), which can achieve a negative SVRE globally. In the CFV-core design parameters (see Tab. 2.1), the SVRE is -0.5 \$ at End of Cycle (EOC).

The idea with the CFV core is that if the sodium starts to boil, the voided

sodium will rise and the sodium plenum will eventually become fully voided. In the worst case, the whole active core is assumed to be voided: all fuel zones, the inner fertile blanket, and the sodium plenum. Liquid sodium is a rather good reflective material for neutrons, but when sodium boils, the density drops drastically, the reflective property fades, and the neutrons will escape through the voided sodium plenum and can be absorbed in the upper shield (see Fig. 2.4). To increase this effect, an inner fertile blanket was introduced. With the inner fertile blanket, the maximum flux will no longer appear in the middle of the active core, but slightly shifted upwards to the upper fissile zone, and therefore increasing the leakage effect through the sodium plenum in case of sodium boiling. To achieve a negative SVRE, this leakage effect has to be larger than the effect of the neutron-spectrum hardening in the fuel.

**Table 2.1:** Main design parameters for the pre-conceptual ASTRID core used [23].

Reactor power (MWth)	1500
Fuel residence Time (efpd* )	1440
Cycle length (efpd)	360
Reloading frequency	4
Average breeding gain per cycle	-0.02
Delayed neutron fraction $\beta$ (pcm)	364
SVRE (\$)	-0.5

\*effective full power day

## 2.3 Reactivity Control Systems for Fast Reactors

Most fast reactor system designs use two shutdown systems [24], the control shutdown system (CSD) and the diverse shutdown system (DSD). The CSD is designed to be used during operation for power shaping and reactivity compensation. During normal conditions the CSD is sufficient for reactor shutdown. The DSD is during normal operation conditions always in parking position in the sodium plenum, and available for scram in case of an emergency shutdown. Both systems have to be able to keep the reactor sub-critical during cold conditions and reloading.

The used control rod designs vary and a number of different absorber materials can be used [25]. However, some similarities can be found, and an example of a typical control rod design can be seen in Fig. 2.5. The control rod absorber region consists of a number of absorber pins, depending on the absorber material. The absorbing part of the control rod (compared with the fuel subassemblies) consists of an outer and an inner wrapper tube. The outer wrapper tube is defining the subassembly itself, and is axially fixed. The inner wrapper tube encases the absorbing pins, and moves together with the absorbing pins. Axially, the typical fast reactor control rod consists of three axial zones: the coolant rich follower, the

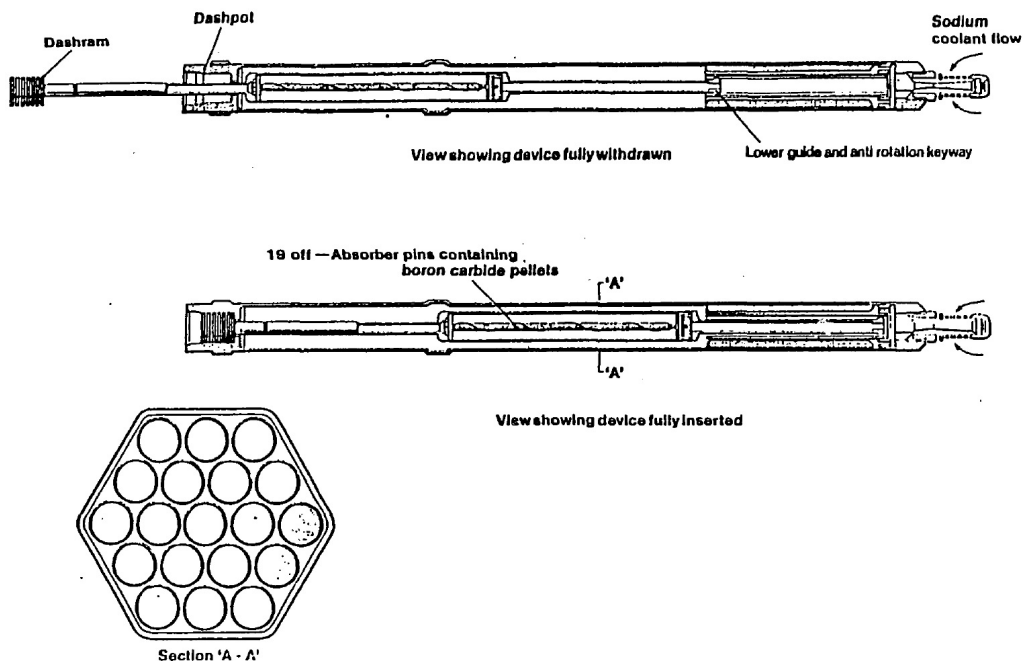


Figure 2.5: An example design of a fast reactor control rod [27].

absorber region, and a stainless-steel rich driver mechanism. The follower consists of some kind of guide piston (see Fig. 2.5), used to help insertion through the fixed control rod subassembly in case of deformed subassemblies. The absorber region can, in the case of boron carbide ( $B_4C$ ) as the absorbing material, consist of a number of different zones with different boron-10 content, in order to optimize the amount of enriched  $B_4C$  used versus the cost [26].

The modeling of the control rods have two main important parameters to consider, the reactivity worth, and the capture rates. The reactivity worth is the main parameter since reactivity control is the purpose of the control rods. However, the capture rates will have different aspects of interest depending on the absorber material used [24]. Ultimately, the capture rates in the absorber will determine the depletion of the absorber material, and thereby their lifetime (typically a couple of years). In case of boron as the absorber, the main capture reaction is the  $(n,\alpha)$  reaction and a helium build-up will occur, and consequently cause swelling of the pins. Another capture rate-related parameter is the induced radioactivity in the absorber material. This is most prominent in absorber materials such as europium and tantalum, where the capture reaction is the  $(n,\gamma)$  reaction. However, a small induction of radioactivity will be induced in boron as well through the  $(n,T,2\alpha)$  reaction. These different neutron captures will lead to different heat generation rates in the absorber, hence the need for heat removal will be different for different absorber materials.

Some fast reactor designs are equipped with some kind of passive reactivity safety system, controlled for instance by a large temperature increase in the coolant [28, 29, 30]. Most of these systems are designed to replace one or a couple of fuel

pins in some fuel subassemblies, not a whole assembly like the control rods, making some of these systems difficult to model in deterministic codes. These kind of systems are not investigated or further discussed in this thesis.

In previous SFR modeling (like *Superphénix*), a homogeneous control rod model was considered combined with a flux weighting scheme (see Sec. 3.1.1). This type of homogenization schemes resulted in discrepancies between calculated values and measured data, with an overestimation of the CRW of over 25% [12]. The main cause of these overestimations was found to be the use of diffusion theory and the neglecting of the heterogeneity effect in the homogenization of the control rods [31]. With an upgrade to transport codes and an improved control rod modeling (see Sec. 3.3), the discrepancies were reduced to  $\pm 5\%$ . For the ASTRID project, the aim is to have the same error margin for the CRW as found in the *Superphénix* experience, with a maximum of  $\pm 5\%$  discrepancy.

### 2.3.1 The Control Rod Systems in the CFV core

In this work, the absorbing material used is  $B_4C$ , since it is the preferred choice for the CFV core, and the design is based on [23]. The control rod absorber region consists of 19  $B_4C$  pins, in a vented stainless steel cladding. Both rod designs (CSD and DSD) consist of two axial absorber zones (see Fig. 2.4): the lower zone containing low boron-10 content, and the upper zone with a higher boron-10 content. The main design parameters for the control rods used in this work are summarized in Tab. 2.2. The CSD rods used in this work consist of natural  $B_4C$  in the lower zone, and  $B_4C$  with a 48% boron-10 content in the upper zone.

This work mainly focuses on the absorber part of the control rod. Hence the follower and the driver mechanism are only described as a homogeneous mixture of sodium and stainless steel, and none of the smaller structural components (such as plugs) are modeled.

**Table 2.2:** Geometrical parameters for the control rods used in the CFV core.

	CSD	DSD
Number of subassemblies	12	6
Lower absorbing length (cm)	60	20
Upper absorbing length (cm)	20	60
Lower boron-10 content (%)	19.9	48.8
Upper boron-10 content (%)	48.8	90

# CHAPTER 3

## Methodology

*This chapter gives an overview of the present calculation procedures regarding neutronics in nuclear reactors, as well as the computational tools used in this work. The latter part covers the derivation of the equivalence procedure and the implementations of the procedure used.*

### 3.1 Neutron Calculations

One of the most important physics parameters inside the nuclear reactor to determine is the neutron flux. To calculate the neutron flux, two different methods can be used: probabilistic or deterministic.

The probabilistic approach uses Monte Carlo techniques simulating one neutron at a time, tracking its life and the life of any secondary neutrons created by the initial neutron. The solution is obtained by running a large number of neutron histories, thereby obtaining a distribution of the neutron flux and an estimate of the statistical error. With Monte Carlo based methods, extensive details can be put into the geometrical description, the neutron energy spectrum, and the material compositions of the system. When enough neutron histories are used, the statistical error can be reduced and reliable results are obtainable. However, to achieve reliable results, computer clusters and long computational times (days or even weeks) are needed for large systems, and this "only" for steady state conditions, hence transients scenarios are not an option as of now for industrial applications.

The deterministic approach is based on solving the Boltzmann transport equation [32], which in steady state can be written as:

$$\begin{aligned} \vec{\Omega} \cdot \vec{\nabla} \psi(\vec{r}, \vec{\Omega}, E) + \Sigma_t \psi(\vec{r}, \vec{\Omega}, E) = & \\ \int_0^\infty dE' \int_{(4\pi)} d^2\Omega' \Sigma_s(\vec{r}, \vec{\Omega}' \rightarrow \vec{\Omega}, E' \rightarrow E) \psi(\vec{r}, \vec{\Omega}', E') & \quad (3.1) \\ + \frac{1}{k} \frac{\chi(E)}{4\pi} \int_0^\infty dE' \nu \Sigma_f(\vec{r}, E') \phi(\vec{r}, E'), & \end{aligned}$$

where  $\psi(\vec{r}, \vec{\Omega}, E)$  is the angular neutron flux as a function on space ( $\vec{r}$ ), direction

( $\vec{\Omega}$ ), and energy ( $E$ ),  $\phi(\vec{r}, E) = \int_{(4\pi)} d^2\Omega' \psi(\vec{r}, \vec{\Omega}', E)$  the scalar flux,  $\Sigma$  macroscopic cross section with subscript  $t$ ,  $s$  and  $f$  (corresponding to total, scattering and fission, respectively),  $k$  the effective multiplication factor,  $\chi$  the energy distribution of fission neutrons, and  $\nu$  the mean number of neutrons released per fission.

The standard deterministic calculation schemes use a two step approach [33]: the homogenization step, and the nodal core calculation. The homogenization step can consist of several model sizes, from single fuel pins to a number of fuel subassemblies, where the geometries are heterogeneously described. The subassembly model are most often performed in a  $2D$  geometry, in order to be able to describe the assemblies radially. With such small models, the homogenization step can use a much finer discretization regarding energy, space, and angle. With the neutron flux obtained from the heterogeneous model, the cross sections can be condensed (averaging in energy) and homogenized (averaging in space), for preparation to the subsequent core calculation. Another important part done in the homogenization step is the depletion calculations, where a number of different isotopes are tracked as a function of time as discrete depletion steps, hence obtaining a cross section library for depleted fuel.

In the second step, the core calculation, the homogeneous cross sections from the homogenization step are used to build up a  $3D$  model of the core. The core calculations are usually performed with a coarse spatial and energy mesh (compared with the homogenization step). The angular dependency is most commonly handled with the diffusion approximation. However other angular approximations are available, such as spherical harmonics ( $P_N$ ), simplified spherical harmonics ( $SP_N$ ), or discrete ordinate ( $S_N$ ) [34]. In the core calculation step, the behavior of the reactor is calculated, such as the power, and one tracks the burnup of the different fuel subassemblies. In this approach, transients (time dependent) cases can also be studied.

The main advantage of the deterministic approach compared with the probabilistic approach is the computer power needed, where results can be obtained on an ordinary desktop computer within minutes with the deterministic approach.

### 3.1.1 Homogenization Methods

To homogenize cross sections, a number of different methods can be used [35], which are most often based on flux-volume weighting:

$$\Sigma_{hom} = \frac{\int dV \Sigma(\vec{r}) \phi(\vec{r})}{\int dV \phi(\vec{r})}. \quad (3.2)$$

The flux-volume weighting in Eq. (3.2) preserves the reaction rates from the heterogeneous description to the homogeneous description. However, methods based on flux-volume weighting will not preserve the eigenvalue ( $k$  in Eq. (3.1)) between the heterogeneous and homogeneous descriptions. In thermal systems,

where diffusion theory is mostly used for the core calculations, this can be solved by introducing discontinuity factors [35, 36]. For other angular approximations, such as higher order  $P_N$  or  $S_N$ , the approach of discontinuity factors is not well defined and not easily used.

Other homogenization methods used are adjoint flux weighting [37] and Superhomogenization [38]. However, most methods focus on homogenizing for diffusion theory, and on fuel regions, not on non-fissile construction materials or control systems.

For fast reactor systems, the flux-volume based homogenization for control rods along with the use of diffusion theory, were the causes of the large discrepancies found between the calculated and the measured CRW in *Superphénix* [12]. To deal with this issue, a reactivity preserving method was introduced, henceforth denoted as the equivalence procedure. In Sec. 3.3 the equivalence procedure is further discussed, and is the homogenization method used throughout this work.

Recent work has been utilizing the previously mentioned Superhomogenization for control rod homogenization [39], which, like the equivalence procedure, takes into account the heterogeneous structure of the control rod. However, this was applied to a homogeneous core, using a radial 2D model, and not applied to a heterogeneous core, such as the CFV core. The scope of this thesis is to evaluate the impact the axial heterogeneities have on the control rod model, and where (radial) 2D based methods are not adequate.

## 3.2 Computational Tools

In this work, a number of different neutronic codes were used, both deterministic and probabilistic. The results in this thesis are presented in a 33 energy group structure, commonly used for fast reactor calculations [40]. All calculations were performed at room temperature and beginning of life (BOL) conditions. The room temperature was chosen for simplicity where neither Doppler broadening nor material swellings were included. The BOL conditions represent fuel where no fission products are present (no burnup), and the fertile blankets are plutonium free. These conditions have been used in order to minimize the possible causes for discrepancies when comparing the deterministic and the Monte Carlo results.

### 3.2.1 ERANOS 2

The ERANOS code package [41] is a collection of deterministic codes used for fast reactor calculations. The codes used within ERANOS during this work includes: ECCO [42], BISTRO [43], and VARIANT [44].

ECCO is a lattice code, based on 2D collision probabilities. In this work, ECCO is used to generate homogeneous cross sections for the fuel, and constructional

materials such as the plenum and reflector. ECCO is also used as part of the equivalence procedure (see Sec. 3.4).

BISTRO is a 2D finite difference transport code with a  $S_N$  angular approximation. In this work, BISTRO is the base of the classical equivalence procedure in ERANOS, used in Chapter 4.

VARIANT is a 3D finite difference nodal code, capable of both diffusion,  $SP_N$ , and  $P_N$  angular approximations. In this work, VARIANT is used for all core simulations of the CFV core (Chapter 6).

### 3.2.2 PARIS

The PARIS code [45], uses the 3D finite element solver SNATCH, which is based on an  $S_N$  angular approximation. In this work, the equivalence procedure has been implemented in PARIS in order to utilize its 3D  $S_N$  solver. In Chapters 5 and 6, PARIS is used to generate equivalent homogenous cross sections for the control-rod absorber, using the equivalence procedure.

### 3.2.3 TRIPOLI-4<sup>®</sup>

TRIPOLI-4<sup>®</sup> (T4) [46] is a continuous energy Monte Carlo code, developed by the CEA. In this work, T4 has been used as a reference tool for the core calculations (Chapter 6).

## 3.3 Homogenization with Reactivity Equivalence

The equivalence procedure used for control rod homogenization is based on two descriptions of the control rod and its surrounding environment: one in which the control rod is heterogeneously described, and one where the control rod is homogeneously described. In both descriptions, the surrounding environment is homogeneously described. Schematic geometries of such models can be seen in Fig. 3.1. With these two models, perturbation theory can be used to derive the equations needed for the homogenization.

### 3.3.1 Derivation of the Equivalence Procedure

To arrive at the equations needed for homogenization by reactivity equivalence, a couple of definitions and derivations are needed. First the Boltzmann transport equation and its adjoint representation is needed so that the exact formulation of the classical perturbation can be obtained [32]. Perturbation theory can be used to see how a small change in the input parameters, as the cross sections or the

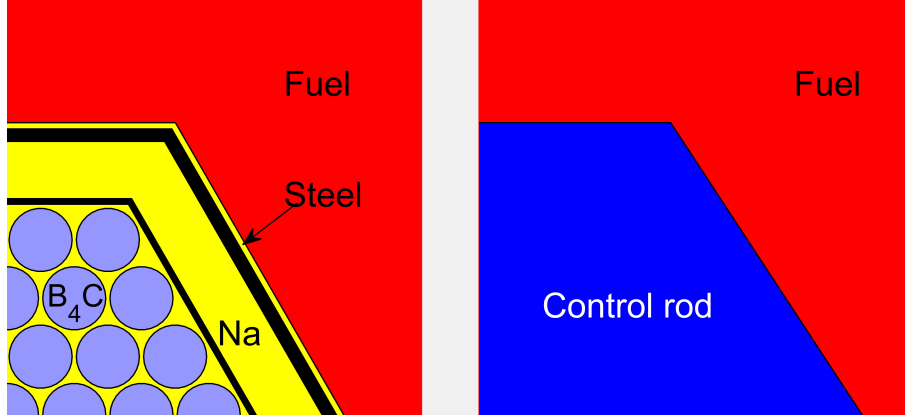


**Figure 3.1:** Schematic geometries of the heterogeneous (left) and the homogeneous (right) descriptions of the models used in the equivalence procedure.

geometry, changes the behavior (reactivity) of the system. For the purpose of homogenization, the exact formulation of the classical perturbation theory can be used to derive equations for homogeneous cross sections to preserve the reactivity, needed for the equivalence procedure.

The (direct) Boltzmann transport equation (3.1) can be written in operator form as [32]:

$$\left( \mathbf{A} - \frac{\mathbf{F}}{k} \right) \psi = 0, \quad (3.3)$$

where  $\psi$  is the angular flux and presented both in continuous energy representation, i.e. Eq. (3.4a,b) and multigroup theory, i.e. Eq. (3.4c,d) as:

$$\begin{aligned} \mathbf{A}\psi &= \vec{\Omega} \cdot \nabla \psi(\vec{r}, \vec{\Omega}, E) + \Sigma_t \psi(\vec{r}, \vec{\Omega}, E) \\ &\quad - \int_{(4\pi)} d^2\Omega' \int_0^\infty dE' \Sigma_s(\vec{r}, \vec{\Omega}' \rightarrow \vec{\Omega}, E' \rightarrow E) \psi(\vec{r}, \vec{\Omega}', E'), \end{aligned} \quad (3.4a)$$

$$\mathbf{F}\psi = \frac{\chi(E)}{4\pi} \int_0^\infty dE' \nu \Sigma_f(\vec{r}, E' \rightarrow E) \phi(\vec{r}, E'), \quad (3.4b)$$

$$\begin{aligned} \mathbf{A}\psi &= \vec{\Omega} \cdot \nabla \psi_g(\vec{r}, \vec{\Omega}) + \Sigma_t^g \psi_g(\vec{r}, \vec{\Omega}) \\ &\quad - \int_{(4\pi)} d^2\Omega' \sum_{g'} \Sigma_s^{g' \rightarrow g}(\vec{r}, \vec{\Omega}' \rightarrow \vec{\Omega}) \psi_{g'}(\vec{r}, \vec{\Omega}'), \end{aligned} \quad (3.4c)$$

$$\mathbf{F}\psi = \frac{\chi_g}{4\pi} \sum_{g'} \nu \Sigma_f^{g'}(\vec{r}) \phi_{g'}(\vec{r}), \quad (3.4d)$$

The adjoint flux is needed as well as the direct flux ( $\psi$  in Eq. (3.3)) for the exact formulation of the classical perturbation theory. A self-adjoint operator  $M$  is defined as [32]:

$$\langle \phi, M\psi \rangle = \langle \psi, M\phi \rangle, \quad (3.5)$$

where for our purpose, the inner product is defined as:

$$\langle \phi, \psi \rangle = \int_0^\infty dE \int_V dV \int_{(4\pi)} d^2\Omega \phi(\vec{r}, \vec{\Omega}, E) \psi(\vec{r}, \vec{\Omega}, E). \quad (3.6)$$

However, the Boltzmann transport equation is not self-adjoint, and an adjoint operator is needed, fulfilling:

$$\langle \phi^\dagger, M\psi \rangle = \langle \psi, M^\dagger \phi^\dagger \rangle. \quad (3.7)$$

With this definition, the adjoint Boltzmann transport equation can be defined as [32]:

$$\left( \mathbf{A}^\dagger - \frac{\mathbf{F}^\dagger}{k} \right) \psi^\dagger = 0, \quad (3.8)$$

where  $\psi^\dagger$  is the adjoint angular flux and

$$\begin{aligned} \mathbf{A}^\dagger \psi^\dagger &= -\vec{\Omega} \cdot \nabla \psi^\dagger(\vec{r}, \vec{\Omega}, E) + \Sigma_t \psi^\dagger(\vec{r}, \vec{\Omega}, E) \\ &\quad - \int_{(4\pi)} d^2\Omega' \int_0^\infty dE' \Sigma_s(\vec{r}, \vec{\Omega} \rightarrow \vec{\Omega}', E \rightarrow E') \psi^\dagger(\vec{r}, \vec{\Omega}', E'), \end{aligned} \quad (3.9a)$$

$$\mathbf{F}^\dagger \psi^\dagger = \frac{\nu \Sigma_f(\vec{r}, E)}{4\pi} \int_0^\infty dE' \chi(E') \phi^\dagger(\vec{r}, E'), \quad (3.9b)$$

$$\begin{aligned} \mathbf{A}^\dagger \psi^\dagger &= -\vec{\Omega} \cdot \nabla \psi_g^\dagger(\vec{r}, \vec{\Omega}) + \Sigma_t^g \psi_g^\dagger(\vec{r}, \vec{\Omega}) \\ &\quad - \int_{(4\pi)} d^2\Omega' \sum_{g'} \Sigma_s^{g \rightarrow g'}(\vec{r}, \vec{\Omega} \rightarrow \vec{\Omega}') \psi_{g'}^\dagger(\vec{r}, \vec{\Omega}'), \end{aligned} \quad (3.9c)$$

$$\mathbf{F}^\dagger \psi^\dagger = \frac{\nu \Sigma_f^g}{4\pi} \sum_{g'} \chi_{g'}(\vec{r}) \phi_{g'}^\dagger(\vec{r}), \quad (3.9d)$$

in continuous (3.9a,b), and multigroup representation (3.9c,d), respectively.

To get the expressions needed for the perturbation theory, a small perturbation is added to the adjoint system:

$$\left( \mathbf{A}^* - \frac{\mathbf{F}^*}{k^*} \right) \psi^* = \left( \mathbf{A}^\dagger - \delta \mathbf{A} - \frac{\mathbf{F}^\dagger - \delta \mathbf{F}}{k - \delta k} \right) (\psi^\dagger + \delta \psi), \quad (3.10)$$

where the perturbed flux  $\psi^*$ , which in a first order approximation is  $\psi^\dagger$  i.e.  $\delta \psi = 0$  in Eq. (3.10). The perturbed  $1/k^*$  term can be expressed in a more usable way as:

$$\begin{aligned} \frac{1}{k^*} &= \frac{1}{k - \delta k} \\ &= \frac{1}{k - \delta k} + \frac{1}{k} - \frac{1}{k} \\ &= \frac{-\delta k}{kk^*} + \frac{1}{k} \\ &= \Delta \rho + \frac{1}{k}. \end{aligned} \quad (3.11)$$

To be able to use the inner product (Eq. (3.6)) and to derive the exact formulation of the classical perturbation theory, two fluxes are needed. Hence, Eq. (3.10) is multiplied with  $\psi$  and integrated, and Eq. (3.3) is multiplied with  $\psi^\dagger$  and integrated. Taking the difference between the two inner products, the following expression can be found:

$$\langle \psi^\dagger, (\mathbf{A} - \frac{\mathbf{F}}{k})\psi \rangle - \langle \psi, (\mathbf{A}^* - \frac{\mathbf{F}^*}{k^*})\psi^\dagger \rangle = 0. \quad (3.12)$$

Finally, by combining and rearranging Eq. (3.11) and (3.12), the expression for the exact formulation of the classical perturbation theory can be written as:

$$\langle \psi^\dagger, \left( \mathbf{A} - \mathbf{A}^* - \frac{1}{k}(\mathbf{F} - \mathbf{F}^*) \right) \psi \rangle - \Delta\rho \langle \psi, \mathbf{F}^* \psi^\dagger \rangle = 0. \quad (3.13)$$

With the exact formulation of the classical perturbation theory, the equations needed for the homogenization can be derived. Within this work, only a non fissile material is homogenized (the control rod), and reactivity equivalence is sought ( $\Delta\rho = 0$ ), hence Eq. (3.13) can be simplified to:

$$\langle \psi^\dagger, (\mathbf{A} - \mathbf{A}^*) \psi \rangle = 0. \quad (3.14)$$

By assuming that the heterogeneous model (left in Fig. 3.1) is the reference system, and the homogeneous model (right in Fig. 3.1) is the perturbed system, term by term, Eq. (3.14) can be solved for the sought  $\mathbf{A}^*$ . As can be seen in Eq. (3.9c),  $\mathbf{A}^*$  consists of the total cross section  $\Sigma_t$  and the scattering cross section  $\Sigma_s^{g \rightarrow g'}$  in the "perturbed" state.

For consistency, the total cross section is not calculated directly through Eq. 3.14, but rather as the sum of its components (in multigroup formalism) as:

$$\Sigma_t^g = \Sigma_c^g + \sum_{g'} \Sigma_{s0}^{g \rightarrow g'}. \quad (3.15)$$

The equivalent capture cross section which appears in Eq. (3.15) can, without any additional approximations, be derived as:

$$\Sigma_{c,hom}^g = \frac{\int_V dV \Sigma_{c,heter}^g(\vec{r}) \int_{(4\pi)} d^2\Omega \psi_g^\dagger(\vec{r}, \vec{\Omega}) \psi_g(\vec{r}, \vec{\Omega})}{\int_V dV \int_{(4\pi)} d^2\Omega \psi_g^\dagger(\vec{r}, \vec{\Omega}) \psi_g(\vec{r}, \vec{\Omega})}. \quad (3.16)$$

To deal with the angular dependence of the scattering cross sections (see Eq. (3.4c)), a Legendre expansion is used for the scalar product of the angles, i.e.  $\mu = \vec{\Omega} \cdot \vec{\Omega}'$ , leading to:

$$\Sigma_s^{g \rightarrow g'}(\vec{r}, \mu) = \sum_{l=0}^{\infty} \frac{2l+1}{4\pi} \Sigma_{sl}^{g \rightarrow g'}(\vec{r}) P_l(\mu), \quad (3.17)$$

$$\Sigma_{sl}^{g \rightarrow g'}(\vec{r}) = \int_{-1}^1 \Sigma_s(\vec{r}, \mu) P_l(\mu) d\mu, \quad (3.18)$$

where  $P_l$  are the Legendre polynomials, which fulfill the following relations:

$$\int_{-1}^1 P_l(\mu)P_k(\mu)d\mu = \frac{2\delta_{l,k}}{2l+1}, \quad (3.19)$$

$$P_l(\vec{\Omega} \cdot \vec{\Omega}') = \sum_{m=-l}^l Y_{lm}(\vec{\Omega})\bar{Y}_{lm}(\vec{\Omega}'), \quad (3.20)$$

where  $Y_{lm}(\Omega)$  is the spherical harmonics, of order  $l$  and  $m$ , and  $\bar{Y}_{lm}(\vec{\Omega}')$  its complex conjugate.

Combining Eq. (3.14), (3.4), and adding Eq. (3.17) and (3.19) yields:

$$\begin{aligned} & \int_V dV \int_{(4\pi)} d^2\Omega \int_{(4\pi)} d^2\Omega' \Sigma_s^{g' \rightarrow g}(\vec{r}, \vec{\Omega}' \cdot \vec{\Omega}) \psi_{g'}(\vec{r}, \vec{\Omega}') \psi_g^\dagger(\vec{r}, \vec{\Omega}) \\ \stackrel{(3.17)}{=} & \int_V dV \int_{(4\pi)} d^2\Omega \int_{(4\pi)} d^2\Omega' \sum_{l=0}^{\infty} \Sigma_{sl}^{g' \rightarrow g}(\vec{r}) \frac{2l+1}{4\pi} P_l(\vec{\Omega} \cdot \vec{\Omega}') \psi_{g'}(\vec{r}, \vec{\Omega}') \psi_g^\dagger(\vec{r}, \vec{\Omega}) \\ \stackrel{(3.19)}{=} & \int_V dV \int_{(4\pi)} d^2\Omega \int_{(4\pi)} d^2\Omega' \sum_{l=0}^{\infty} \Sigma_{sl}^{g' \rightarrow g}(\vec{r}) \frac{2l+1}{4\pi} \times \\ & \sum_{m=-l}^l \frac{4\pi}{2l+1} Y_{lm}(\vec{\Omega}) \bar{Y}_{lm}(\vec{\Omega}') \psi_{g'}(\vec{r}, \vec{\Omega}') \psi_g^\dagger(\vec{r}, \vec{\Omega}) \\ \Rightarrow & \sum_{l=0}^{\infty} \int_V dV \Sigma_{sl}^{g' \rightarrow g}(\vec{r}) \phi_{g'l}(\vec{r}) \phi_{gl}^\dagger(\vec{r}), \end{aligned} \quad (3.21)$$

where

$$\phi_{g'l}(\vec{r}) = \int_{(4\pi)} d^2\Omega \sum_{m=-l}^l \bar{Y}_{lm}(\vec{\Omega}) \psi_{g'}(\vec{r}, \vec{\Omega}), \quad (3.22a)$$

$$\phi_{gl}^\dagger(\vec{r}) = \int_{(4\pi)} d^2\Omega \sum_{m=-l}^l Y_{lm}(\vec{\Omega}) \psi_g^\dagger(\vec{r}, \vec{\Omega}), \quad (3.22b)$$

Using the relation in Eq. (3.21) and (3.14), each equivalent scattering cross section of order  $l$  can be calculated as:

$$\Sigma_{sl, hom}^{g' \rightarrow g} = \frac{\int_V dV \Sigma_{sl}^{g' \rightarrow g}(\vec{r}) \phi_{g'l}(\vec{r}) \phi_{gl}^\dagger(\vec{r})}{\int_V dV \phi_{g'l}(\vec{r}) \phi_{gl}^\dagger(\vec{r})}. \quad (3.23)$$

For  $l = 0$  (where  $Y_{00} = 1$ ), and by including Eqs. (3.22a) and (3.22b), the following expression is obtained:

$$\Sigma_{s0, hom}^{g' \rightarrow g} = \frac{\int_V dV \Sigma_{s0}^{g' \rightarrow g}(\vec{r}, \vec{\Omega}) \int_{(4\pi)} d^2\Omega \psi_{g'}(\vec{r}, \vec{\Omega}) \int_{(4\pi)} d^2\Omega \psi_g^\dagger(\vec{r}, \vec{\Omega})}{\int_V dV \int_{(4\pi)} d^2\Omega \psi_{g'}(\vec{r}, \vec{\Omega}) \int_{(4\pi)} d^2\Omega \psi_g^\dagger(\vec{r}, \vec{\Omega})}. \quad (3.24)$$

By combining Eq. (3.4c) with Eq. (3.15), it can be seen that the zero-order self scattering term  $\Sigma_{s0,hom}^{g \rightarrow g}$  appears twice, once in the total cross section and once in the scattering integral. Hence, Eq. (3.23) is modified and the self scattering cross section for  $l = 0$  is calculated as:

$$\Sigma_{s0,hom}^{g \rightarrow g} = \frac{\int_V dV \Sigma_{s0}^{g \rightarrow g}(\vec{r}) \left[ \int_{(4\pi)} d^2\Omega \psi_g(\vec{r}, \vec{\Omega}) \int_{(4\pi)} d^2\Omega \psi_g^\dagger(\vec{r}, \vec{\Omega}) - \int_{4\pi} d^2\Omega \psi_g^\dagger(\vec{r}, \vec{\Omega}) \psi_g(\vec{r}, \vec{\Omega}) \right]}{\int_V dV \left[ \int_{(4\pi)} d^2\Omega \psi_g(\vec{r}, \vec{\Omega}) \int_{(4\pi)} d^2\Omega \psi_g^\dagger(\vec{r}, \vec{\Omega}) - \int_{4\pi} d^2\Omega \psi_g^\dagger(\vec{r}, \vec{\Omega}) \psi_g(\vec{r}, \vec{\Omega}) \right]} \quad (3.25)$$

## 3.4 Implementation

It can be seen in Eqs. (3.16) and (3.23) that the sought homogeneous cross sections are dependent on the homogeneous adjoint flux, which in turn is dependent on the homogeneous cross sections. This dependence calls for an iterative procedure to solve the problem, where the adjoint flux will be updated in each iteration. Throughout this thesis, two implementations are used, the older ERANOS implementation (in Chapter 4), and the new PARIS implementation (in Chapters 5 and 6). Both utilize the same basic calculation scheme, and the PARIS calculation scheme can be seen in Fig. 3.2. The two implementations have some slight differences:

1. the neutronic solver, used for the flux calculations
2. the initial adjoint flux used
3. some fix-ups for stability and convergence (see Sec. 3.4.1)

The input of the user consists of: the composition for each medium, the geometry of the system, and the cross section library. From these, ECCO is used to calculate self-shielded cross sections for the absorbing material, the sodium and stainless steel mixture in the rest of the control rod, and the surrounding materials.

Both implementations uses a Cartesian geometry, where the original circular and hexagonal geometry (Fig. 3.1) is approximated with a Cartesian geometry, seen in Fig. 3.3. To compensate for the change in volume between the two descriptions of the system, the density ( $D$ ) in the Cartesian geometry is corrected as:

$$D_{cart} = \frac{V_{org}}{V_{cart}} D_{org}, \quad (3.26)$$

to keep the number of atoms identical in both geometries.

With the geometry and the self-shielded cross sections from ECCO, the heterogeneous system is solved (in ERANOS with BISTRO, and in PARIS with SNATCH) acquiring the direct flux  $\psi_{het}$ . The PARIS implementation solves the adjoint equations for the heterogeneous system, and uses the obtained adjoint flux for the first

homogenization, while the ERANOS implementation uses a flat flux approximation as the adjoint homogeneous flux  $\psi_{hom}^\dagger$  for the first homogenization. After these initial steps, the iteration ( $i$ ) loop is initiated where the calculation steps are as follows:

- Homogenize equivalent cross sections using the direct and adjoint flux, as by using Eqs. (3.16), (3.23), (3.25), and (3.15)
- Solve the adjoint equations for the homogeneous system, updating the adjoint flux  $\psi_{hom}^\dagger$
- Check convergence  $|\rho^{i-1} - \rho^i| < \varepsilon_\rho$

When convergence is achieved in reactivity, one last homogenization is made, to make use of the last updated adjoint flux, and the equivalent homogeneous cross section are saved.

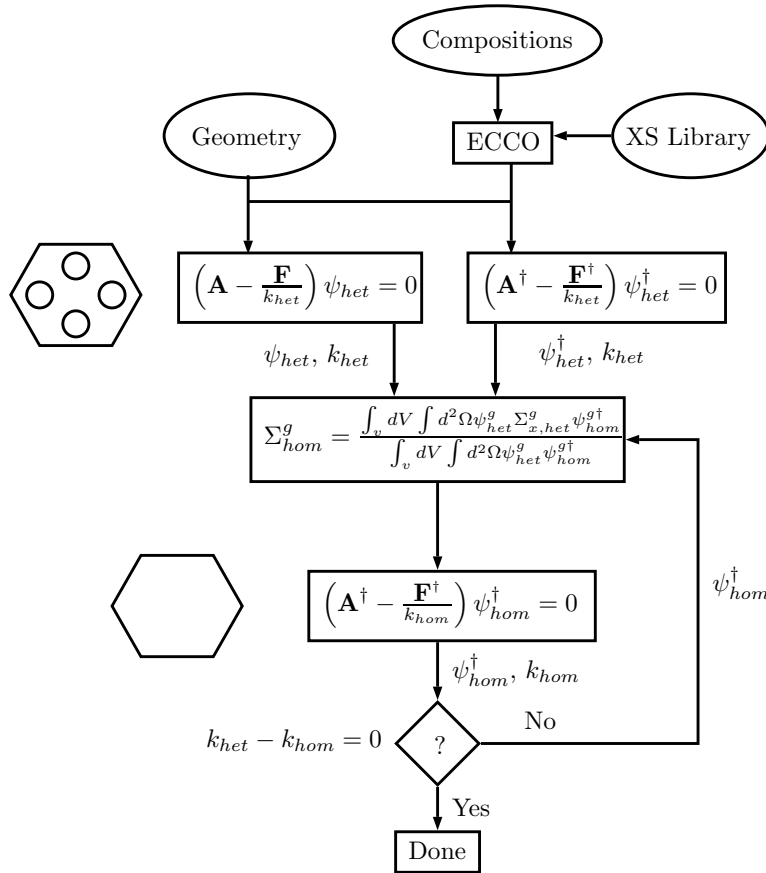


**Figure 3.2:** Calculation scheme used for the equivalence procedure in the PARIS implementation.

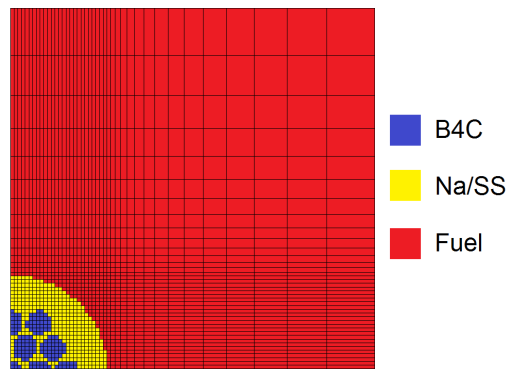
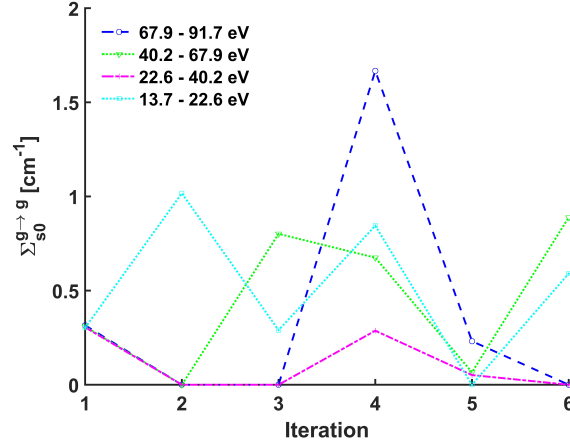


Figure 3.3: The Cartesian geometry used in the equivalence procedure

### 3.4.1 Numerical Stability Enhancement

The self-scattering is the most dominant reaction type in the control rod (see Sec. 3.5). When calculating the self-scattering cross section by Eq. (3.25), a minus sign is present between two integrals. In some cases, this minus sign will give rise to a negative (and unphysical) self-scattering cross section, and in the worst case, even a negative total cross section. In addition to the unphysical results, this effect will jeopardize the stability and convergence of the equivalence procedure.

In any implementation of the equivalence procedure, these negative self-scattering cross sections need to be handled in some way in order to have a stable procedure. In the ERANOS implementation, this was handled by a fix-up that consisted of setting the self-scattering cross section to zero in case of negative results from Eq. (3.25). This kind of fix-up is not uncommon, and will help the procedure to yield results and converge. However, this fix-up might yield non-reliable results in some cases. In case the fix-up is used in an intermediate iteration (not the last homogenization), the next homogeneous system will be solved with cross sections where in certain energy groups, the self scattering is zero. The new homogeneous adjoint flux will for these groups be very high, causing in turn very large self-scattering cross sections in the next iteration. Another source of this behavior is in case the integral in (3.25) is positive but close to zero. These types of behavior might give rise to an oscillating nature of some self-scattering cross sections. The procedure may still converge in reactivity, but the cross section in some energy groups might be fairly random, or zero (if the last homogenization yielded negative self scattering cross sections). In the worst cases, these unphysical cross sections might even crash the neutronic solver, and no solution will be obtained. An example of such oscillations can be seen in Fig. 3.4, for four energy groups. In Fig. 3.4 both examples of instabilities can be seen, most commonly with zero values (in most iterations), but also a small value for the self-scattering cross-section at iteration 5 for the 40.2-67.9 eV and 22.6-40.2 eV energy groups.



**Figure 3.4:** Oscillations seen in different iterations for four different energy groups, using the ERANOS implementation with its fix-up.

In the PARIS implementation, another fix-up was introduced, where Eq. (3.25) was modified to handle the negative self-scattering cross section, by using the absolute value of the integral differences as:

$$\Sigma_{s0,hom}^{g \rightarrow g} = \frac{\int_V dV \Sigma_{sl}^{g \rightarrow g}(\vec{r}) \left| \int_{(4\pi)} d^2\Omega \psi_g(\vec{r}, \vec{\Omega}) \int_{(4\pi)} d^2\Omega \psi_g^\dagger(\vec{r}, \vec{\Omega}) - \int_{(4\pi)} d^2\Omega \psi_g^\dagger(\vec{r}, \vec{\Omega}) \psi_g(\vec{r}, \vec{\Omega}) \right|}{\int_V dV \left| \int_{(4\pi)} d^2\Omega \psi_g(\vec{r}, \vec{\Omega}) \int_{(4\pi)} d^2\Omega \psi_g^\dagger(\vec{r}, \vec{\Omega}) - \int_{(4\pi)} d^2\Omega \psi_g^\dagger(\vec{r}, \vec{\Omega}) \psi_g(\vec{r}, \vec{\Omega}) \right|} \quad (3.27)$$

This fix-up will ensure that negative self scattering cross sections will never appear, and prevent the integrals to end up with very small values.

To compare the two fix-ups, the final self-scattering cross section from the case found in Fig. 3.4 and the result from the PARIS implementation with the fix-up from Eq. (3.27), can be seen in Fig. 3.5. It should be noted that the largest value of the ERANOS results (at  $10^{-4}$  MeV) reaches  $11 \text{ cm}^{-1}$ . It can be seen in Fig 3.5 that for the ERANOS implementation in three energy groups, the self-scattering cross section is zero, hence Eq. (3.25) yielded negative cross sections in three energy groups in the last iteration. Below  $2 \cdot 10^{-4}$  MeV, none of the values are reliable, and are entirely results of the ERANOS fix-up. With the new fix-up introduced in the PARIS implementation (Eq. (3.27)), this behavior is no longer observed. One can also notice that for high energies (above  $unit[10^{-2}]MeV$ ), the fix-up in Eq. (3.27) generates slightly higher self-scattering cross sections, compared with the ERANOS implementation.

The impact of the absolute value in Eq. (3.27) is not investigated further, due to the very uncommon cases in which the procedure can be used without any fix-up, making an analysis of these impacts very difficult.

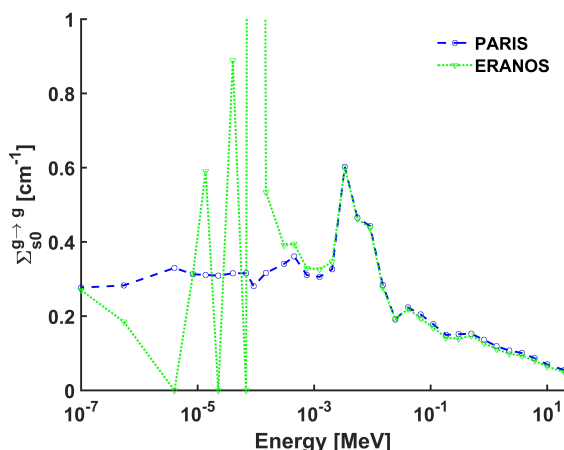


Figure 3.5: Resulting self-scattering cross sections for the two different implementations.

### 3.5 The Classical Equivalence Procedure

As a basis in this work, the results from the classical equivalence procedure (radial 2D (X-Y) geometry) are used as a representation of how the procedure is used classically. The classical equivalence procedure uses a model where a control rod is radially surrounded by homogeneous fuel, as was seen in Figs. 3.1 and 3.3.

For the classical equivalence procedure, the resulting cross sections can be seen in Fig. 3.6, where it can be observed that the main reaction is the self scattering, and the sought capture is but a small part of the total cross section, even in low energy regions. The reason for this can be seen in the corrective factors which are defined as:

$$f = \frac{\Sigma_{equivalent}}{\Sigma_{flux-volume}}, \quad (3.28)$$

where  $\Sigma_{equivalent}$  is the equivalent cross section, and  $\Sigma_{flux-volume}$  is the flux-volume weighted cross section based on a homogeneous control rod description (Eq. (3.2)). The corrective factors are used for tracking in which energy groups the equivalence procedure has the largest impact. The corrective factors for the capture cross sections, and the  $B_4C$  capture cross section can be seen in Fig. 3.7, where the difference from the flux-volume weighted cross sections are the largest for low energies. This arises since the neutron flux and the adjoint flux are low in the  $B_4C$  pellets in the low energy groups.

In Chapter 6, this 2D (X-Y) model is used as a representation of how the procedure is classically used. In Chapters 4 and 5, a model that is representative of the studies made is used (a 1D model in Chapter 4, and a 2D (X-Z) model in Chapter 5). The classically generated equivalent control rod cross sections in a fuel environment are denoted TEXS (Traditional Equivalent Cross Section) throughout the thesis.

In Chapters 5 and 6, only the PARIS implementation is used, always with

the fix-up presented in Eq. (3.27), in order not to introduce differences from the different neutronic solvers and fix-ups (as was observed in Fig. 3.5).

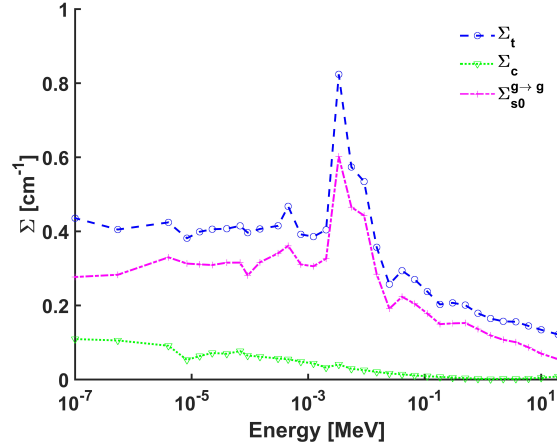


**Figure 3.6:** The resulting equivalent cross sections (total, capture, and self scattering), from the classical 2D X-Y model with a fuel surrounding. The calculation was performed with the PARIS implementation of the equivalence procedure.

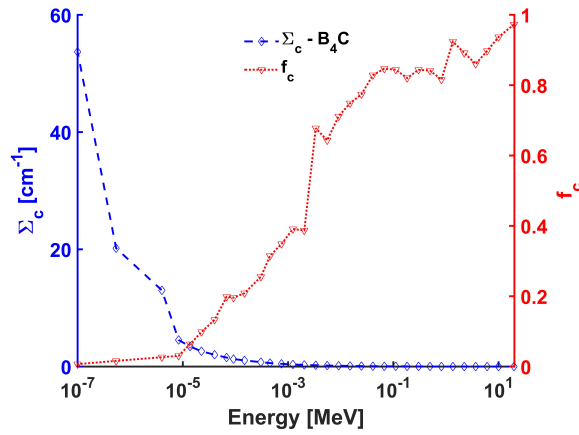


**Figure 3.7:** Corrective factors for the equivalent capture cross sections (found in Fig. 3.6) and the capture cross sections for the B<sub>4</sub>C pellets.

## CHAPTER 4

# Spectral Impact on Cross Sections

*This chapter describes the spectral shifts that occur in an SFR, and investigates the impact that the spectral shifts have on the equivalent homogeneous control-rod cross sections. This chapter is based on, and summarize Paper I, in which more details can be found.*

### 4.1 Spectral Shifts

The SFR uses a fast neutron spectrum, as can be seen in Fig. 4.1. However, the neutron spectrum is not uniform over the whole core. In a critical reactor, the neutron spectrum has its main contribution from the Watt spectrum [47], which is the spectrum with which neutrons were born (in the fission process). The spectrum is then shaped depending on how the neutrons are scattered and absorbed in different media.

The adjoint flux, also known as the neutron importance [32], describes the usefulness of a neutron, i.e. whether it will be able to induce fission or not. As seen in Fig. 4.1, in the fuel of an SFR, the spectrum of the neutron importance is largest at high energies and at low energies, and correlates to where the neutron has the highest probability to induce a fission in the fuel (See Fig. 2.2 for the fission cross-

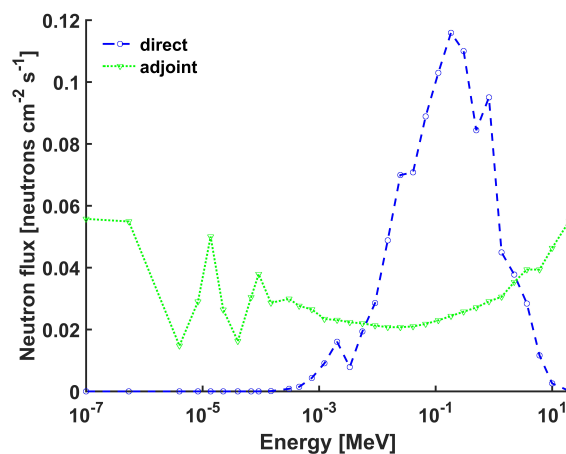


**Figure 4.1:** The direct and adjoint flux in a typical SFR fuel assembly.

section of Pu-239). In a non-fissile medium, the neutron importance will harden with increasing distance from the fissile medium. This hardening is explained by the fact that further away from the fissile medium, low energy neutrons have much lower probability to scatter back into the fissile medium, compared with high energy neutrons, which will have a larger probability to scatter into the fissile medium, and thereby may cause a fission.

Since the equivalence procedure uses both the direct neutron flux and the adjoint neutron flux to homogenize the control-rod cross sections (Sec 3.3), it is important to know how spectral variations affect the homogenized control-rod cross sections.

The main parameter determining the equivalent cross sections is of course the control rod itself. However, this work focuses on the surrounding material and the impact the environment surrounding the control rod absorber has on the homogeneous equivalent control-rod cross sections. In the classical *2D* equivalence procedure, the control rod is surrounded by fuel (as seen in Fig. 3.1), hence the important environmental parameters will be the fuel subassembly composition, i.e. the plutonium content, and fuel/coolant ratio. In cases in which a non-fissile medium surrounds the control rod, like the sodium plenum, the modeling is not as simple with the classical *2D* equivalence procedure, since no fissile material is present and a neutron source is needed.

To enforce a spectral shift in the vicinity of a control rod, in order to study the impact spectral shifts have on the equivalent control-rod cross sections, a *1D* model was used. In this simple model, a transition zone was introduced between the fuel and the control rod, as can be seen in Fig. 4.2. By increasing the length of the transition zone, the neutron spectrum experiences a stronger softening, since more scattering events will take place before the neutrons reach the control rod. Instead of varying the length of the transition zone, the composition can be modified, and material dependencies can be investigated. These two mechanisms

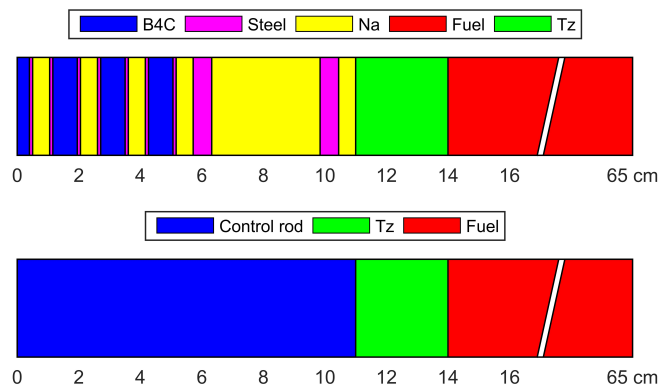


**Figure 4.2:** Example *1D* geometry of a control rod, with fuel sandwiching a transition zone (Tz).

cannot be studied totally independently, since when introducing a new material, the volumetric ratios of the transition zone will change, and depending on the cross sections of the new medium and its atomic weight (lethargy gain for neutrons in each scattering event), a change in the softening effect will be seen. Therefore, care has to be taken in order to distinguish these mechanisms.

## 4.2 Impact of Resonances

One of the mechanisms altering the neutron spectrum is obtained by adding a medium, for which the isotopes have wide resonances. To determine the impact the wide resonances have on the resulting equivalent control rod cross sections, a 30 cm thick graphite transition zone was added. Graphite was chosen since its cross sections do not vary significantly with energy, and do not contain any large resonances, hence a uniform softening of the neutron spectrum will take place. By introducing a small amount (5%) of a foreign isotope, containing one or two wide resonances, the impact the resonance has on the resulting equivalent cross sections can be studied. Four different isotopes were studied, and a summary of their main resonances, and main usage in a SFR, can be found in Tab. 4.1.

**Table 4.1:** Isotopes tested, with their main resonances and where they can be found in a SFR.

Isotope	Resonance energy [MeV]	Main usage
O-16	$4.35 \cdot 10^{-1}$	Oxide fuel and MgO reflector
	1.0	
Na-23	$2.8 \cdot 10^{-3}$	Coolant
Mg-23	$8.3 \cdot 10^{-2}$	MgO reflector
	$2.57 \cdot 10^{-3}$	
Fe-56	$2.8 \cdot 10^{-2}$	Main isotope in stainless steel

Comparing the system with pure graphite in the transition zone and the systems where a small amount of foreign isotopes has been introduced into the graphite, the difference in the neutron spectrum (at the boundary between the transition zone and the control rod) can be seen in Fig. 4.3, and the difference induced in the resulting equivalent total cross sections by the foreign isotopes can be seen in Fig. 4.4.

As previously mentioned, the spectral changes have two main causes, the slowing down effect and the wide resonances. In Fig. 4.3, the impact of the resonances can clearly be seen for their respective energies, where the neutron flux is reduced in the energy group containing the resonance. The slowing down effect can be seen by looking at how the spectra harden. The spectral hardening is dependent on the atomic weight of the scattering medium. Since all isotopes tested (Tab. 4.1) are heavier than graphite (C-12), all spectra are shifted towards a faster regime.

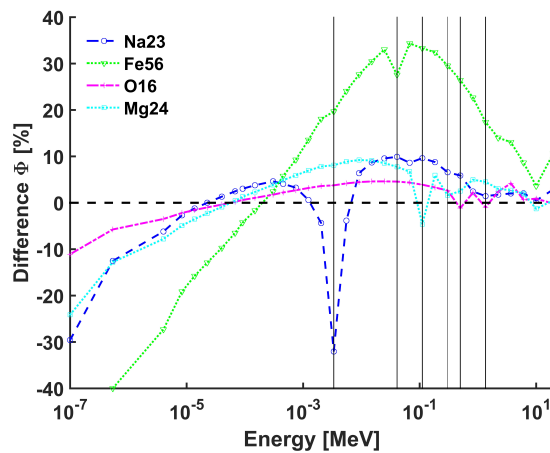


**Figure 4.3:** Difference in neutron spectra in case of a graphite transition zone with small amounts of single isotopes. The black vertical lines indicates the resonances.

In the difference in cross sections seen in Fig. 4.4, the resonance groups can clearly be observed. However, the differences seen in cross section do not follow the same sharp changes as the differences seen in the flux (Fig. 4.3). It can be observed that the cross sections in the energy groups around the resonances also show a substantial change, and in some cases a change as large or even larger than the energy group containing the resonance. This is an effect of the usage of the receiving group in the scattering cross section calculations (Eq. 3.23).

At the highest energy groups, a rapid change can be seen in Fig. 4.4. This is a numerical effect, due to a very low flux level in the high energy group, and the calculation of the cross sections will diverge (division by a small number). This is an effect induced by the transition zone itself. With a lot of scattering in the transition zone, very few neutrons with high energies will reach the control rod.

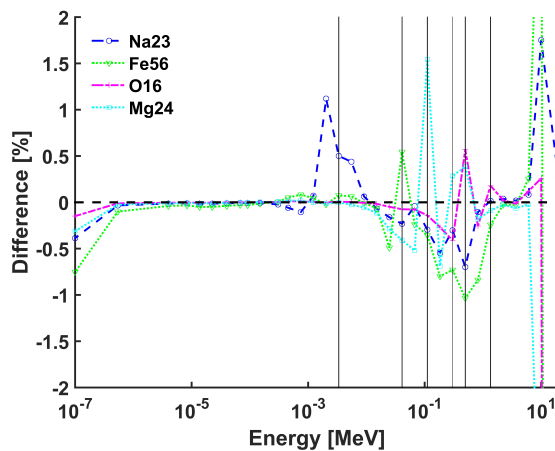


**Figure 4.4:** Errors induced in the total cross section, in case of a graphite transition zone with small amounts of single isotopes. The black vertical lines indicate the resonances.

This effect has to be treated carefully when dealing with materials situated far from a fissile medium.

### 4.3 Impact of Spectral Softening

To determine the impact a softened neutron spectrum has on the equivalent cross sections, a more realistic material was used, compared with the fictive graphite mixtures used in Sec. 4.2. For this purpose, a fresh fertile UOX blanket (no plutonium i.e. low amount of fission neutrons) was chosen as the composition of the transition zone. By varying the length of the transition zone, the control rod will experience different degrees of spectral softening. With four different transition zone lengths: 0 cm (ref), 10 cm, 30 cm, and 50 cm. The neutron spectra at the interface between the transition zone and the control rod can be seen in Fig. 4.5, and the difference in total cross section, compared with a system without a transition zone (transition zone length of 0 cm), can be seen in Fig. 4.6.

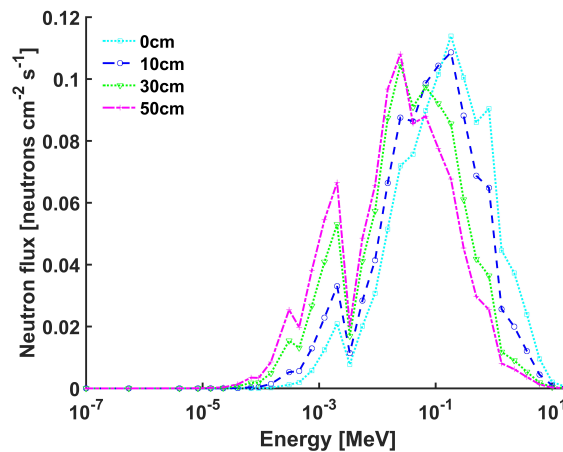


**Figure 4.5:** Neutron spectra for different lengths of transition zone containing a fertile blanket.

It can be seen in Fig. 4.5 that with each increase of the transition zone length, the neutron spectra get softer and more distorted, due to the down-scattering of neutrons and the reduced amount of fissions in the fertile material. For all spectra, in two energy groups, the flux is more or less stable. By comparing Fig. 4.5 and 4.3, it can be noted that these are the energy groups that contain the wide resonances from Na-23 and Fe-56, which are both present in the fertile UOX blanket.

In the changes seen in equivalent cross sections (Fig. 4.6), two effects can be seen: the transition zone length independent peaks in the  $10^{-6} - 10^{-4}$  MeV region, and the transition zone length dependent changes in the  $10^{-2} - 1$  MeV region. The independent peaks in the low energy region are, as described in the previous section (Sec. 4.2), caused by wide resonances, in this case from different uranium, plutonium, and americium isotopes. The length-dependent changes, induced by

the softening of the spectrum, represent a much slower process than the changes induced by the resonances. After a 10 cm transition zone, the maximum change is less than 2%, and after 30 cm, differences of 3-5% can be seen. The changes induced between transition zone lengths of 30-50 cm are very small, indicating that the effect of spectral softening reduces with distance.

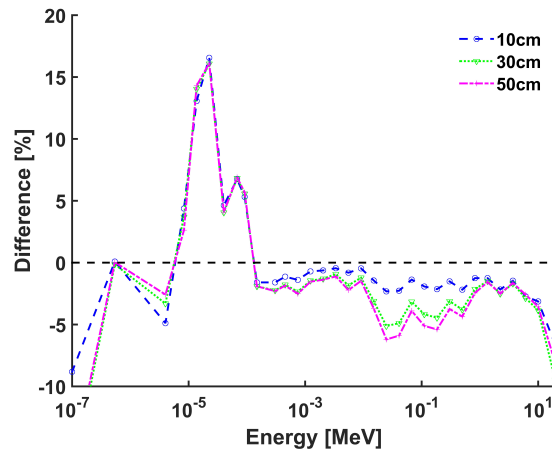


**Figure 4.6:** Difference in total cross section for different lengths of transition zone containing a fertile blanket.

## CHAPTER 5

# Characterization of Axial Regions

*This chapter summarizes Paper II, in which more examples and details can be found. The main goal of this chapter is to identify, by simple models, regions where the axial heterogeneities found in the CFV core will affect the control rod. These results will help to find quantitative approximations for the full core model.*

### 5.1 Control Rod Environments

The CFV core consists of a number of different materials and material interfaces (seen in Fig. 2.4), which the control rod will experience at different axial positions. To distinguish between all these different environments, they can be divided into three groups: *radial environments*, *core interfaces*, and *axial control rod interfaces*. The radial environments and the core interfaces are fixed since they are part of the core, and hence can be grouped as core environments. The axial control rod interfaces are not stationary, and change with the control rod position.

In the CFV core used in this work, the main radial environments found in Fig. 2.4 that the control rod will experience are: the two fissile zones, the inner fertile blanket, and the gas and sodium plena. These environments have different neutronic properties, where the fissile zones are highly absorbing with production of fission neutrons, the fertile blanket is highly absorbing but with low fission neutron production, and the plena, which are characterized by high scattering and low absorption. These main radial environments can in turn be combined to form a number of core interfaces, such as the interface between the fissile zone and the fertile blanket. The axial control rod environments can be found at the interfaces between the absorbing part and the structural part of the control rod, as the follower and driver, and in the case of different  $B_4C$  zones with different boron-10 content within the absorber (see Fig. 2.4). The different environments found in the CFV core are summarized in Tab. 5.1, together with the abbreviations used in this thesis.

Since the control rod can be moved from its parking position, in the sodium plenum, down to the fully inserted position, the absorber will experience all the different core environments and interfaces listed in Tab. 5.1. In addition, the axial control rod interfaces, when moved through the core, will experience different

**Table 5.1:** The different environments found in the CFV core, with the abbreviations used. When two abbreviations are given, the first letter determines the radial environment of that segment.

Type	Description	Abbreviation
Radial Environment ( <i>E</i> )	Fissile	<i>f</i>
	Plenum	<i>p</i>
	Fertile blanket	<i>b</i>
Core Interface ( <i>I</i> )	Fissile/Fertile blanket	<i>f/b, b/f</i>
	Fissile/Plenum	<i>f/p, p/f</i>
Axial Control Rod Interface ( <i>S</i> )	Absorber/Follower	<i>abs/follower</i>
	Natural boron/48% Boron-10	<i>na/48, 48/na</i>
	48% Boron-10/90% Boron-10	<i>48/90, 90/48</i>
	Absorber/Driver	<i>abs/driver</i>

core environments depending on the control rod position. Thereby, combined environments will emerge, which in turn are new unique environments for the control rod. These combined environments will create a vast amount of different environments and yield a unique neutron spectrum within the control rod for each combination, thereby changing the equivalent homogeneous control-rod cross sections. To reduce the amount of homogenizations needed to a manageable amount, qualified approximations are needed.

In the previous chapter (Chapter 4), the impact a change in the spectrum has on the equivalent cross section was investigated, with the abrupt response from the wide resonances, and the more far reaching softening effect. For this investigation, an axial 2D (X-Z) model is used, since the 1D model previously used is not representative of the environments listed in Tab 5.1, and the range of impact these environmental changes have cannot be assessed with such a simplified model. With all the possible environments that emerge due to the combined environments, all cases cannot be investigated in the same detail, and therefore, a few representative models are chosen for further studies.

The first model used represents one of the axial control rod interfaces (the follower/absorber interface) for which a correct modeling is of great importance, especially during operating conditions, when the control rod is just slightly inserted into the core. A 60 cm model (axially), with reflective boundary conditions on both at the top and the bottom ( $z = 0$  cm, and  $z = 60$  cm), is used, where the control rod is placed between 30-60 cm with a follower below (0-30 cm); radially (x-direction) the control rod and follower are surrounded by fuel solely.

To evaluate the core environments, a 150 cm model (axially) of the CFV core (Fig. 2.4) was used, with a control rod extending through the whole core, with no axial control rod interfaces. This kind of control rod is not realistic, but is used to obtain a model independent of the axial control rod interfaces. At the top and the bottom of the model ( $z = 0$  cm, and  $z = 150$  cm), a black boundary condition is applied.

## 5.2 Means of Characterization

To investigate where the reliability of the classical equivalence procedure can be questioned, a number of methods can be used. Studying the neutron spectrum, as was done in Chapter 4, will no longer be practical, because of the additional dimension introduced. In this work, two characterization techniques were chosen: spectral indicators by microscopic reaction rates, and change in homogeneous reaction rates.

The spectral indicators used in this work is based on microscopic reaction rates defined as:

$$\bar{\sigma}_x^i = \frac{\sum_g \sigma_{x,i}^g \phi_g}{\sum_g \phi_g}, \quad (5.1)$$

where  $\bar{\sigma}_x^i$  is the spectral indicator,  $\sigma_{x,i}^g$  the microscopic cross section,  $i$  the isotope, and  $x$  the reaction. Throughout this work, the spectral indicator used is the ratio between the U-238 capture and U-235 fission rates:

$$I_{U235f}^{U238c} = \frac{\bar{\sigma}_c^{U238}}{\bar{\sigma}_f^{U235}}. \quad (5.2)$$

This spectral indicator was chosen since it is an indicator that increases with an epithermal flux, and it can be measured in a reactor. In general, the used spectral indicator will have its minimum values when surrounded by fuel, and with a softer spectrum, it will increase. Worth noticing is that for a thermal neutron spectrum, this spectral indicator will decrease, since there are no resonances in  $\sigma_{c,U238}$  at thermal energies, while  $\sigma_{f,U235}$  increases for thermal energies.

The typical SFR control rod (Fig. 3.1) can radially be divided into two regions, the *inner* region, where the absorbing materials are located, and the *outer* region, which contains sodium and the wrapper tubes. These two regions are quite different from a neutronic point of view, where the inner region is characterized by high absorption (and will affect the capture cross section in the homogenization), and the outer is characterized by high scattering. The spectral indicator will yield one value per mesh point, and by taking the mean value for each axial plane over the inner and outer regions of the control rod, two axial distributions are obtained and can thus be studied.

The homogeneous reaction rates are calculated as:

$$R_t = \sum_{I \subset V} \sum_g \Sigma_{hom}^g \phi_g^I, \quad (5.3)$$

where  $\Sigma_{x,hom}^g$  is the equivalent homogeneous cross sections. Presented in this Chapter are the total reaction rates, calculated in each axial level, with two different sets of cross sections: the environmentally corrected equivalent cross sections (ECXS) and the TEXS. The TEXS are generated in a small X-Z *model* in a fuel

environment, representing the results from Sec. 3.5. The ECXS are generated in the previously described  $X$ - $Z$  models, for each axial level. However, a stability issue was found when homogenizing multiple axial levels at the same time. To handle this issue, one axial level was homogenized at a time.

## 5.3 Interface Characteristics

### 5.3.1 Absorber/Follower Interface

The spectral indicators for the absorber/follower interface can be seen in Fig. 5.1, where the left side (0-30 cm) represents the follower and the right side (30-60 cm) represents the absorber.

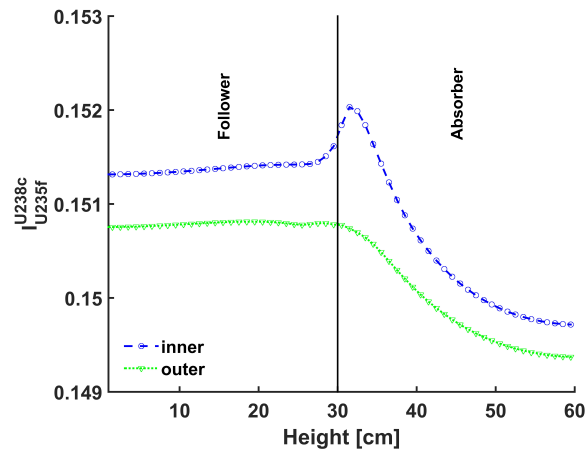


**Figure 5.1:** The  $I_{U_{235f}}^{U_{238c}}$  spectral indicators at the follower/absorber interface.

It can be seen that the spectral indicators are stable in the follower region, then increase in close proximity to the absorber. The increase at the interface can be seen as a hardening of the neutron spectrum, since the low energy neutrons will quickly be absorbed in the  $B_4C$ , hence leading to an increase of the spectral indicator. The hardening continues within the absorber some distance from the follower, up to 20 cm from the interface.

The total reaction rates are presented in Fig. 5.2, where TEXS shows a constant behavior throughout the absorber, even in the presence of a spectral shift at the interface with the follower. With the ECXS on the other hand, a large effect close to the interface can be seen, where the difference between the two is over 12%. The main differences observed between the TEXS and the ECXS can be seen 10-15 cm from the interface.

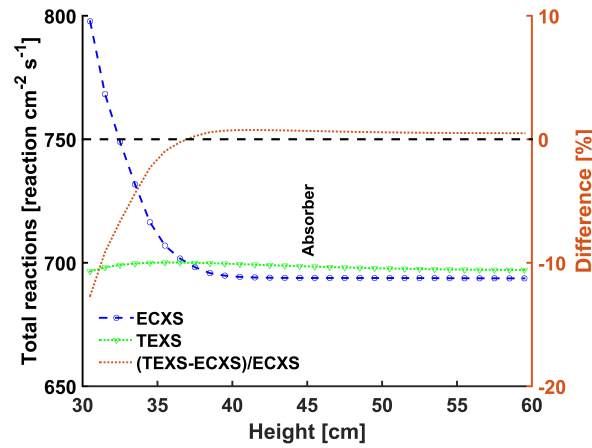


Figure 5.2: The total reaction rates at the follower/absorber interface.

### 5.3.2 Core Environments

In Fig. 5.3, the axial distribution of the spectral indicators can be seen for the core environments. The spectral indicators are varying all over the core, have a smooth behavior, and the indicators for the inner and outer regions follow the same pattern, except in the plena, where the indicators for the two regions differ. It can be seen that the lower fissile zone (30-55 cm) does not, even in the center, reach the same spectral hardness as the upper fissile zone (75-110 cm). This effect is explained by the farther reaching of the slowing down effect (see Sec. 4.3), combined with the fact that the upper fissile zone is 10 cm higher than the lower fissile zone. However, the impact of the interfaces cannot easily be determined just by the spectral indicators themselves. In order to clearly expose the spectral changes close to the interface, the derivative of the spectral indicators has to be studied. This is presented in Fig. 5.4.

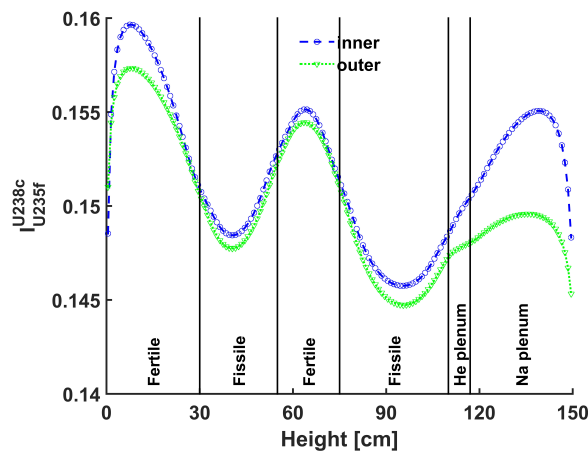
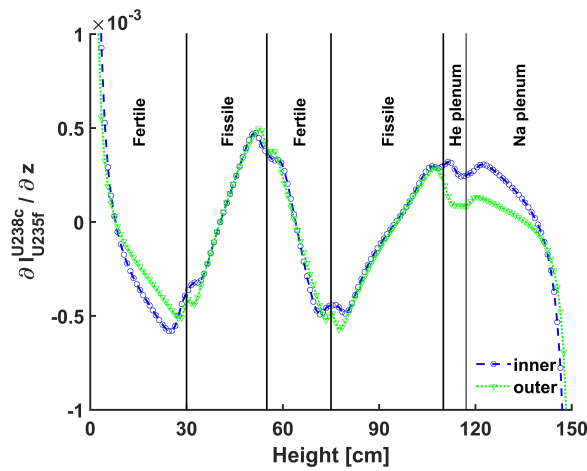


Figure 5.3: The  $I_{U235f}^{U238c}$  spectral indicators for the core environments.

In the derivative of the spectral indicators, irregularities are observed around each environment interface. Since these irregularities are the product of both the slowing down and the resonance effect (Sec. 4.2), the exact impact of each respective contribution is difficult to determine. However, these irregularities are sufficient to determine the range of the main (short range) spectral impact around the core interfaces. At the fissile/fertile interfaces (at 30 cm, 55 cm, and 75 cm), the irregularities have a range of about 5 cm on both sides of the interface, with a slightly farther reach for the inner region. The spectral shift occurs outside the control rod, and will therefore affect the outer region first hand. The inner region will experience the spectral shift from the environment after yet another spectral shift in the outer region, hence the farther reach can be seen as a second order effect.



**Figure 5.4:** The derivative of the spectral indicators  $\frac{\partial I_{U_{238c}}^{U_{235f}}}{\partial z}$  for the core environments.

The total reaction rates can be seen in Fig. 5.5, presented for the homogeneous system, calculated with TEXS, ECXS, and the difference between the two. Within the fuel zones, an offset can be seen between the two results, slightly larger in the lower fissile zone. In the upper fissile zone (most representative of the classical procedure), the discrepancy increases close to the interface. Similarly to the irregularities in the derivative of the spectral indicators (see Fig. 5.4), the range of these discrepancies is of about 5 cm from the material interfaces. As can be expected, in all non-fuel zones, the discrepancies increase.

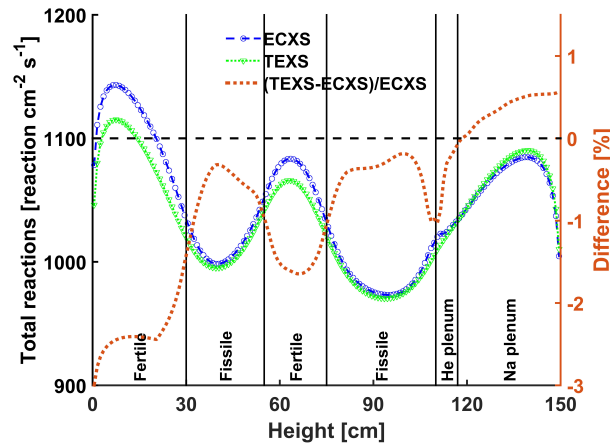


Figure 5.5: Total reaction rate for the core environments.

## 5.4 Remarks

The main discrepancies between the TEXS and the ECXS could be seen at the follower/absorber interface, not in any core environment. This effect can be explained by the location of the material interface. When the environment changes outside the control rod (i.e. the core environments), the neutron spectrum will change for the outer absorbing pins. However, the inner pins will be somewhat shielded from the spectral change by the outer pins, hence being less susceptible to the spectral change in an exterior environment. If the material change occurs internally instead, a part of this shielding effect of the inner pins disappears, where the worst case is for the follower/absorber interface, where the inner pins are directly connected to the low absorbing follower. Therefore, a much larger effect is seen for the internal control rod interfaces, compared with the core environments. Similar effects are to be expected at the driver/absorber interface (see Fig. 2.4).

For the core environments, the main impact of the spectral shifts could be found in the first 5 cm from an interface. Since the spectral change occurs at first hand close to the outer part of the control rod, the range of 5 cm is very similar to the mean free path of neutrons in the outer part (5.4 cm).

The offset seen in the reaction rates (Figs. 5.2 and 5.5) can have multiple explanations, including the approach of homogenizing one axial level at a time.



# CHAPTER 6

## Impact on Core Parameters

*This chapter describes the impact the spectral shifts have on important control rod related core parameters, through the homogenization of the control rods. This chapter is based on and summarizes Papers III & IV, and only covers the most important results.*

### 6.1 Control Rod Related Parameters

The control rods in the CFV core represent the only mechanism used for reactivity control, shut down, and power shaping. For the safety assessments of a core, the shut down margin has to be predicted accurately, so that a safe shut down can be assured during different scenarios. Thus, the reactivity effect of the control rod (the CRW) is the most vital of the control rod related parameters. The reactivity will be presented in  $\$$  which is defined in  $\$ = \rho/\beta$ . For the *Superphénix* reactor, for which the classical equivalence procedure was experimentally tested, the error found in the CRW was  $\pm 5\%$  [12], the same error margin is set for the CFV core. The CRW is calculated as:

$$CRW = \rho_j - \rho_{ref}, \quad (6.1)$$

where  $\rho_j$  is the reactivity at control rod position  $j$ , and  $\rho_{ref}$  is a reference reactivity. Usually,  $\rho_{ref}$  is taken at the parking position of the control rods, but since the error is sought for all positions, the reference position used in this thesis is when the control rods are withdrawn past the upper protection (see Fig. 2.4), hence the core will only experience the follower.

Another important reactivity parameter is the SVRE. Since the CFV core is designed to have a negative SVRE, as described in Sec. 2.2.1, the effect the control rod cross sections has on the SVRE is studied and is calculated as:

$$SVRE = \rho_{voided} - \rho_{nominal}. \quad (6.2)$$

Besides the reactivity effects, different reaction rates are important for different types of subassemblies. For the  $B_4C$  control rods, the capture rate (the  $(n,\alpha)$  reaction) is the most important reaction rate, since it determines the boron depletion and the swelling of the  $B_4C$ , hence its lifetime (see Sec. 2.3). The equivalence procedure is however not constructed to preserve the reaction rates (as the flux-volume

weighted cross sections are), but is still important to study. In the fuel subassemblies the fission rate is most important, since this determines the power output as well as the burnup of the fuel. The fuel subassemblies that are neighboring a control rod will be affected by the control rod cross sections. Hence, it is of interest to study the impact of the control rod cross section on the fission rate (or power).

## 6.2 Control Rod Partitioning

With the minimum 5 cm range of the largest spectral impact on the cross section, found in Chapter 5, the 80 cm control rod absorber is divided into eight 10 cm segments, to be able to take all interfaces into account. Based on the results from Chapter 5 the following approximations and assumptions are made:

- In the sodium plenum, the cross sections are assumed not to change farther than 10 cm away from the fissile zone, and the same cross section set is used for all control-rod segments situated in the plenum. This is also done to avoid the numerical effects at high energies seen in Sec. 4.2, when modeling regions far from a fissile material.
- When a segment is farther away than 5 cm from an interface, the effect of that interface is neglected.
- The effect of the combined environments (eg. axial control rod interface situated at an interface between two core environments) is assumed to act in the same range as in the individual cases.
- When no axial control rod interface is present (as for the follower/absorber), the fissile/fertile interfaces will be treated in the same way.

To investigate the impact the ECXS have on the different core parameters, an S-curve is calculated. An S-curve is defined as the reactivity worth the control rod has in different axial positions. For the S-curve calculation, the whole control rod bank is moved stepwise from the parking position to fully inserted. In this work, a total of eleven different control rod positions have been used, between 210 cm and 120 cm, to form the S-curve. To reduce the number of homogenizations needed, only the CSD rods are studied. However, the results obtained for the CSD rods are transferable to the DSD rods. For a fully inserted control rod, the environments can be seen in Fig. 6.1. Since the axial control rod interfaces move through the core, a number of different environments will arise. For the whole S-curve calculation, 27 unique sets of cross sections are needed (for the CSD rods), which have to be calculated twice, once for the nominal core and one for the voided core, ultimately ending up to 54 unique sets of control rod cross sections.

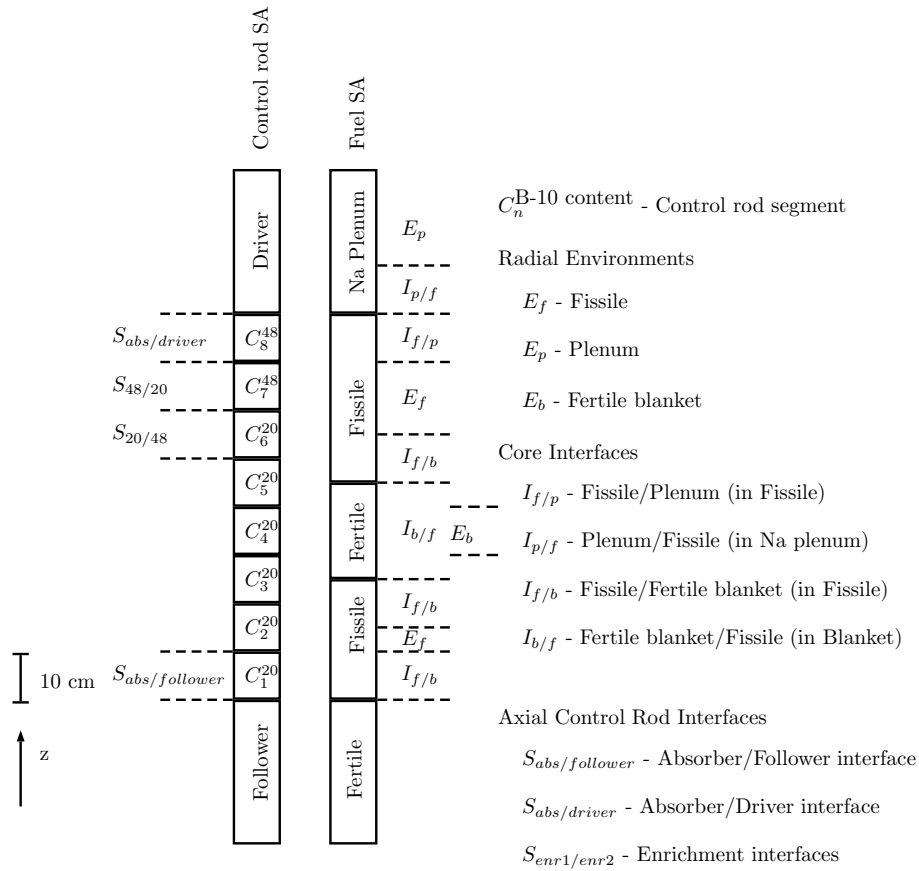


**Figure 6.1:** Partitioning of a fully inserted control rod. The nomenclature can be found in Tab. 5.1

### 6.2.1 Control Rod Homogenization

The cross sections in a fuel environment  $E_f$ , are calculated with the classical 2D equivalence procedure (see Sec. 3.5), while the rest are generated using the 3D implementation of the equivalence procedure (see Sec. 3.4). All 3D models have a size of 20 cm in the X-Y plane, and 60 cm in the axial Z direction. All boundary conditions are reflective, except when a sodium plenum is present in the model, in which a black boundary condition is applied at  $z=60$  cm.

An example of a geometry used for control rod homogenization can be seen in Fig. 6.2, where the follower/absorber interface is modeled at the interface between the fuel and the fertile blanket. In all cross section generations, the PARIS implementation of the equivalence procedure was used (see Sec. 3.4) with the same fix-ups applied, as discussed in Sec. 3.4.1. As was also discussed in Sec. 5.2, only one region could be homogenized at a time due to some stability problems.

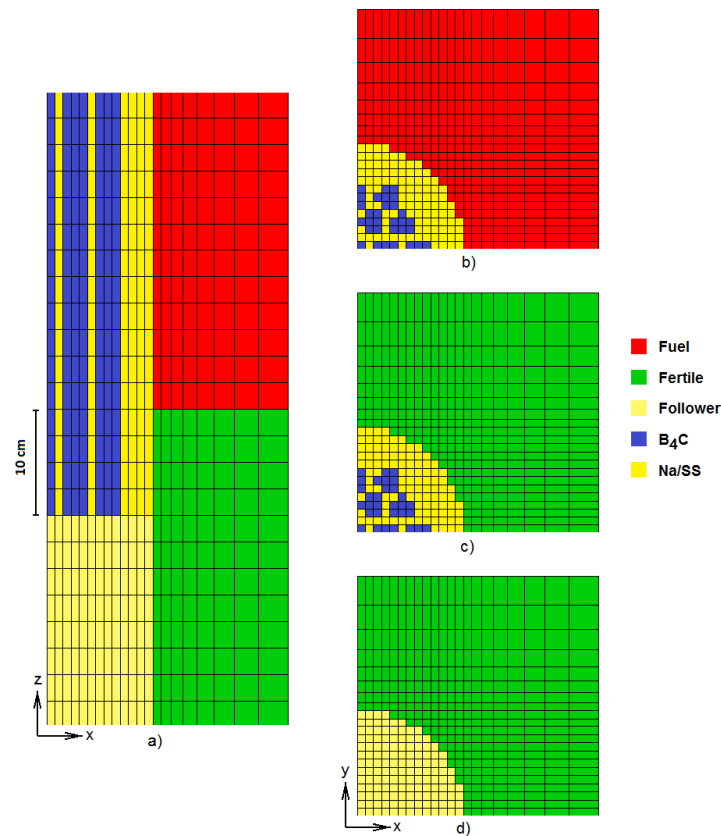


**Figure 6.2:** Geometry of a control rod at the follower/absorber interface, at the core interface between the fissile zone and the fertile blanket. The axial arrangement can be seen in a), the different radial representations for the different axial zones in b), c) and d).

### 6.3 Calculation Route

The presented results use most of the computational tools presented in Sec. 3.2. The equivalent cross sections are prepared with the PARIS code, as described in Sec. 3.4. These cross sections are later used in the VARIANT solver (within the ERANOS code package), for the core calculation. As a reference, a T4 model of the core was used, which was calculated for each control rod position, both for the nominal and voided cores (see Sec. 6.3.1).

For the nominal case, two sets of cross sections are compared, the 2D generated TEXS, and the 3D generated ECXS.

For the voided case, it is assumed that the entire active core is voided (fuel zones, inner fertile blanket and the sodium plenum), and three sets of cross sections are compared, the TEXS, the 3D ECXS in a nominal environment, and the 3D ECXS in the voided environments ( $ECXS_{void}$ ). In all these cases, the sodium is present within the control rod, which is a standard assumption for voided calculations in a SFR.

In order to combine these to evaluate the SVRE, three combinations were used:

- The original procedure, where the TEXS is used for both nominal and voided cases, denoted *TEXS/TEXS*. The voided environment is not taken into account.
- The axial heterogeneities are taken into account using the ECXS for both nominal and voided cases, denoted *ECXS/ECXS*. As in the original procedure, the voided environments are not handled.
- The correct environments are used, where the ECXS are utilized for the nominal case and the  $ECXS_{void}$  for the voided case. This case is referred to as *ECXS/ECXS<sub>void</sub>*.

### 6.3.1 The TRIPOLI-4<sup>®</sup> Reference Model

Since no experimental data are available for a CFV type core, a Monte Carlo model was used as a reference case.

The T4 model uses a heterogeneous description of all the fissile and fertile parts of the fuel subassemblies, as well as the absorbing part of the control rods. The rest of the subassemblies (as reflectors, plena and protection) are homogeneously described, since no structural data for these regions were used in the deterministic approach.

To be able to compare the T4 and VARIANT results, the tallies used in T4 were set to be the same as for the computational mesh in VARIANT, and all reaction rates and fluxes were normalized to power (1500 MW). All T4 calculations were performed with  $5 \cdot 10^8$  neutron histories.

## 6.4 Reactivity Effects

The two T4 reference S-curves and their differential CRW, for the nominal and the voided cores can be seen in Fig. 6.3. From Fig. 6.3, the efficiency of the control rods is shifted downwards in the core in the voided case, because of the increased leakage through the plenum. However, the total CRW is not notably affected by the voided core.

The difference in reactivity for each control rod position in the nominal case can be seen in Fig. 6.4, and for the voided case in Fig. 6.5. In both cases a similar trend can be seen for the TEXS, where a good agreement can be found for the fully withdrawn (210 cm) and fully inserted positions (120 cm). However, when the control rod is slightly inserted around operating positions (180 cm and 190 cm), the maximum discrepancy for the TEXS are found. For the nominal case the maximum error is 4%, but for the voided case the error is over 10%. With the ECXS the effect is damped for both cases at the most exposed positions, and the induced error is reduced. In the voided case (Fig. 6.5), the ECXS reduces the discrepancy, at the

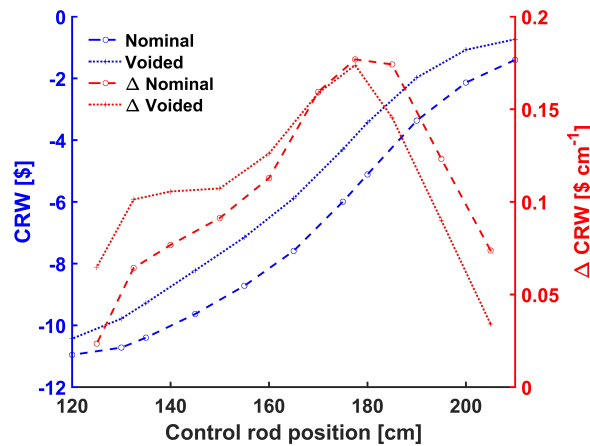


Figure 6.3: The T4 reference S-curve, for both the nominal and voided cases.

worst position (190 cm) to below 6%. Moreover, with  $ECXS_{void}$  the discrepancy is reduced to below 3.5%. It can be seen that the main difference between ECXS and  $ECXS_{void}$ , can be found for control rods slightly inserted into the core, where a majority of the control rod absorber is still in the plenum. With the main bulk of the absorber inserted into the core, only a small difference can be seen. This is because the main difference in material composition can be found in the plenum between the voided and nominal conditions, not in the fuel region.

For both ECXS and  $ECXS_{void}$  (i.e. for both nominal and voided conditions), a large discrepancy can be found at positions within the sodium plenum (210 cm), and this effect will be discussed in more detail in Sec. 6.4.2. However, excluding the 210 cm position, with the fully environmental description for the two cases, the error found never exceeds  $\pm 2.5\%$  in the nominal case and  $\pm 3.5\%$  for the voided case.

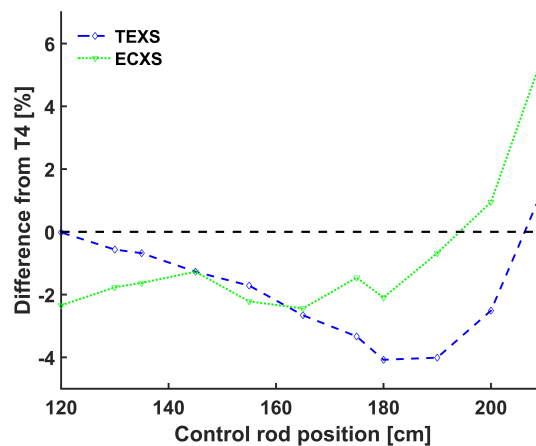


Figure 6.4: Difference in reactivity in the S-curve for the nominal case.

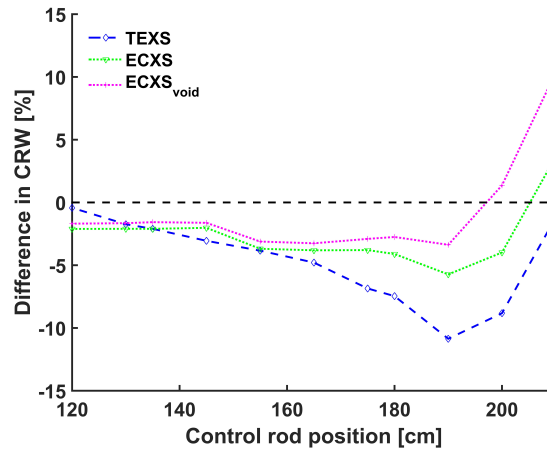


Figure 6.5: Difference in reactivity in the S-curve for the voided case.

### 6.4.1 Reactivity Effect of Individual Environments

By breaking down the ECXS into the separate environments, the impact of the different interfaces can be studied. For this purpose, two different control rod positions (for the nominal case) are chosen, at 180 cm and at 120 cm, respectively. The individual contributions of the different ECXS can be found in Tab. 6.1, where it can be seen that the main contributors to the difference between the TEXS and the ECXS are the axial control rod interfaces, such as the follower absorber interface (at the 180 cm position), and different boron enrichment interfaces (for the 120 cm position). In comparison, the core environments have a small impact on the full ECXS effect. The smallest effect is seen for the fertile blanket, even though the calculations were performed BOL conditions, where the fertile blanket contains no plutonium, thereby enhancing the difference between the fertile and fissile compositions.

Table 6.1: Individual contributions of the ECXS, presented as difference in CRW from the T4 reference.

XS set	$\frac{\Delta CRW}{CRW}$ [%]	
	180 cm	120 cm
Control Rod Position	180 cm	120 cm
T4	-5.13 \$ (ref)	-11 \$ (ref)
TEXS	-4.1	-0.02
Absorber/Follower	-1.1	0.1
Plenum	-5.1	-
Fertile blanket	-	-0.2
Enrichment interfaces	-	-2.1
Full ECXS	-2.1	-2.3

## 6.4.2 Fine Partitioning of the Follower/Absorber Interface

The largest discrepancies found in Sec. 6.4 for the ECXS appear at the top of the core (210 cm). At this control rod position, the absorber is not connected to the fissile zones, and the follower/absorber interface will have the largest impact on the reactivity, hence the modeling of these interfaces will play a large role. As found in Sec. 5.3.1, a large change could be seen for the first 10 cm of the absorber. To take the large changes seen into account, a separate model was used, where instead of the 10 cm segment size of the  $C_1^{nat}$  (see Fig. 6.1), a 2.5 cm partitioning was used. The 3D equivalence procedure was then applied to generate ECXS for these segments.

The investigation was conducted at the 210 cm position, where the discrepancy was the largest for the 3D generated cross sections. The difference in CRW from the T4 reference, for the TEXS and the ECXS with both the 10 cm or the 2.5 cm partitioning, can be seen in Tab. 6.2.

**Table 6.2:** Error in reactivity at the 210 cm control rod position.

Cross section set	$\delta$ CRW [%]
TEXS	1.5
ECXS (10 cm)	5.8
ECXS (2.5 cm)	1.7

By reducing the mesh size of the follower/absorber interface, taking the large spectral gradient found into account (Sec. 5.3.1), the error in CRW for the control rod situated in the sodium plenum is greatly reduced.

It should be noted that when reducing the partitioning size, the effect of the approach of homogenizing one region at a time will increase, and additional errors will be introduced. However, this example shows the significance of the partitioning size at this exceptional environment.

## 6.4.3 Sodium Void Reactivity Effect

The SVRE (Eq. (6.2)) for the reference case and the three investigated cases can be seen in Fig. 6.6, where a large discrepancy of 1 \$ can be found between the reference and the three deterministic cases. This was studied in [48], and was found to be caused by errors in the leakage modeling through the sodium plenum. However, the difference between the three deterministic approaches is small, with a maximum difference of 3% (0.09 \$).

A much larger effect in SVRE can be seen for the control rod position, where the difference in SVRE between different control rod positions is more than 1 \$. The lowest SVRE is found for a control rod inserted through the entire upper fuel zone, and can be considered as a shielding effect. When the control rods are slightly

inserted into the core, the neutron flux is pushed downwards into the core, hence reducing the leakage through the sodium plenum (which is the largest source of leakage for the voided core), and thereby reducing the SVRE.

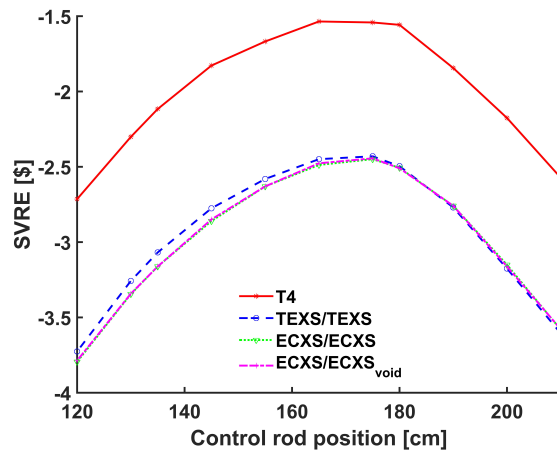


**Figure 6.6:** The SVRE for the reference and the cases obtained with the three different cross section sets.

## 6.5 Impact on Reaction Rate

For the nominal case at the 180 cm control rod position, the capture rates in one of the central control rods can be seen in Fig. 6.7. As indicated in Sec. 5.3.1, the classical equivalence procedure is not able to capture the steep gradient in the absorber close to the follower. With the ECXS, this effect is more accurately predicted (despite the coarse partitioning). However, in the rest of the absorber, the capture rates are underpredicted.

A disadvantage with the ECXS can also be seen in Fig. 6.7, with discontinuities at the boundaries between the different segments. This is an effect arising from assigning different cross sections (for the same material) to the different segments, which are larger than the calculation mesh.

The difference from the T4 reference in the linear power rate (directly connected to the fission rate) for the two sets of cross sections can be seen in Fig. 6.8, with the standard deviation from the T4 results ( $2\sigma_{T4}$ ) given for comparison. It can be seen that, at this control rod position, the linear power rate is slightly reduced with the 3D generated equivalent cross sections, because of the higher capture seen in Fig. 6.7. However, both cases show results within the  $2\sigma_{T4}$  statistical error of the T4 results.

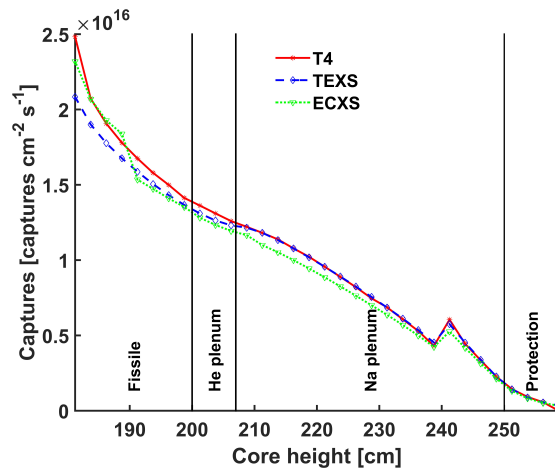


Figure 6.7: Capture rates in a control rod, at critical insertion (180 cm), in the nominal case.

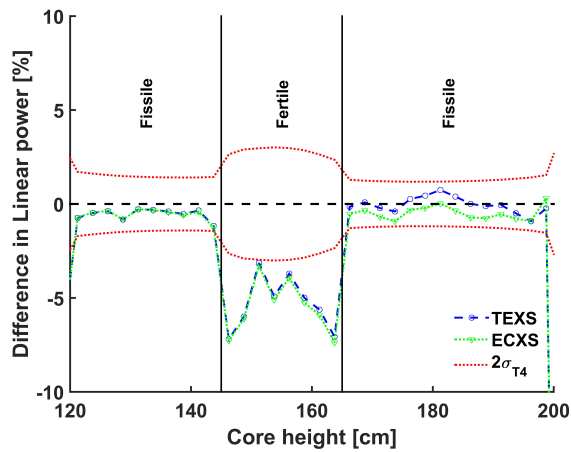


Figure 6.8: Error in Linear Power rate, at critical insertion (180 cm), in the nominal case, for a fuel subassembly adjacent to a control rod.

# CHAPTER 7

## Summary and Future Work

*This final chapter summarizes the results found, as well as highlight some problems found. Most importantly, this chapter contains possible further studies that will bring this field forward.*

### 7.1 Summary

In any type of nuclear reactor, reliable computational tools are needed to be able to predict the core performance, and to perform safety assessments for postulated accident scenarios. In previously built SFRs, the control rod worth was greatly overpredicted, and new computational tools and procedures were needed. In the innovative new designs of fast reactor systems, like the CFV core, a number of different axial zones are utilized to increase the inherent safety features. With the axial heterogeneities found in the CFV core, the performance of the previous procedures for control rod homogenization, is questionable.

To assess how different environments affect the control rod, a series of studies were performed, ranging from simple *1D* models to full *3D* core models.

#### 7.1.1 Impact of Environmental Differences

A simple *1D* model was used to understand how the spectral shifts affect the control rod and the homogenization scheme used. It was found that two different effects had to be regarded: the short range effect of wide resonances, and the more long range effect of the softening of the neutron spectrum.

To identify the regions where these effects were the greatest, some representative CFV environments were investigated in a *2D* model. The largest effects could be found at the interfaces inside the control rod, such as the follower/absorber interface. When the environment changed outside the control rod, a smaller impact was seen, where the main differences could be found at the transition between different materials, and in the sodium plenum. The main changes around a material interface could be localized within 0-5 cm from any interfaces, with some smaller effects seen 5-10 cm from the interface.

Assessing the impact the different control rod cross sections (induced by spectral shifts) have in a CFV core, some of the main core parameters connected to the control rods were investigated. This was done by comparing the classical *2D* procedure and a new *3D* procedure for control rod homogenization, with a Monte Carlo reference. The equivalence procedure was implemented in *3D* so that the different axial interfaces could be modeled while homogenizing the control rod.

Compared with a Monte Carlo reference for a core at nominal conditions, the classical equivalence procedure could recreate the CRW within the requested 5% error margin, with a maximum error margin of 4%. However, at certain control rod positions in a voided core, the results were not within the required error margin, where errors of up to 11% were found for the classical equivalence procedure. With the *3D* equivalence procedure, the errors could be reduced to 2.5% for the nominal case and 3.5% for the voided case. Both procedures were within, or close to, the statistical error from the Monte Carlo reference, when considering the linear power of a fuel assembly next to the control rod.

The SVRE was not greatly affected by the control rod cross sections. However, the control rod position could make a large difference, hence care has to be taken when defining the SVRE, if the SVRE is to be calculated at the most probable control rod position (fully inserted), or at the worst position (half-way inserted).

### 7.1.2 Disadvantages & Complications

With the equivalence procedure in general, a disadvantage can be connected to the need for fix-ups to make the procedure stable. With most fix-ups, changing the integrals or values of the calculated cross sections, the reactivity equivalence will be broken, and complete reactivity equivalence will not be obtained.

A couple of disadvantages with the newly implemented *3D* equivalence procedure can be found, connected to the needed axial discretization. If a coarse partitioning is chosen, discontinuities will arise at the boundaries between different segments. If instead a fine partitioning is used, a large amount of cross section sets are needed, which in turn will increase the computing power needed for the homogenization.

With a finer partitioning, the question arises how much impact only homogenizing one segment at a time will have on the homogeneous cross sections. This approach was used because of instabilities in the implemented equivalence procedure, while homogenizing multiple regions at the same time. Unfortunately, the cause of this instability could not be identified, hence the full extent of the impact the "one region at a time" approach has on the equivalent cross sections could not be assessed. If the cause of these instabilities could be determined, the computational time could be reduced drastically, and a finer partitioning would become more feasible (since multiple ECXS can be generated in each calculation).

## 7.2 Conclusions

In this thesis, a number of spectral shifts a control rod can experience were studied. These spectral shifts arise at different positions in a CFV-type core, because of the different environments. With the spectral shifts, the equivalent control rod cross sections change, and thereby affect the core parameters.

The core environments separate from the fissile environment (fertile and sodium plenum) showed a small effect on the core parameters, and the classical *2D* equivalence procedure yields reliable results at nominal conditions. The only core environment that presented a challenge for the *2D* procedure was for control rods situated in a voided plenum, and in such cases *3D* modeling is recommended.

The largest environmental impacts were found at the axial control rod interfaces, such as the interface between the follower and the absorbing part of the control rod, which is poorly represented by the traditional *2D* (*X-Y*) equivalence procedure, and a more detailed *3D* modeling is advisable.

For other fast reactor concepts, analogous behaviors are to be expected, especially at the axial control rod interfaces, although to a different extent depending on the materials used. However, with new core environments (different reflective materials or blankets) different from the investigated environments, similar studies have to be conducted, especially for materials that cause a large softening effect on the neutron spectrum.

The presence of the effects investigated in this thesis are independent of the homogenization scheme used. However, the performance will not be the same for other homogenization techniques such as the superhomogenization technique.

## 7.3 Outlook

There are a number of possible ways to proceed with the topic of control rod modeling in fast reactor systems, and the most important suggestions, identified in this work, are listed below:

- Reference experiments are recommended, especially regarding the follower/absorber interface, and other material transitions within the control rod, such as transition zones between different boron-10 enrichment.
- A more detailed model of the follower/absorber interface might be required. In this work, the most simple homogeneous model was used. Since the follower/absorber interface is very exposed during operating conditions, the actual steel structure below the absorber will make a difference. This includes the modeling and the cross sections of the follower close to the absorber.

- For a full evaluation of the *3D procedure*, a burnup model (similar to [23]) should be implemented. This should be done with a heterogeneous model, to take into account the shielding effect the outer absorbing pins have on the inner pins, as well as the lack of shielding effect at the follower/absorber interface. This would allow for a better life time assessment of the control rod, and for predicting more accurate conditions during EOC and at the most exposed parts of the absorber.
- To be able to use a *3D* homogenization scheme, resolving the constraint of only homogenizing one region at the time is crucial. It would be of importance to be able to study the effect of a smaller partitioning, as well as the impact the "one region at a time" approach used in this work has. To be noted, the root of this problem might be (neutronic) solver sensitive, as well as the procedure itself.
- In this work, only one homogenization procedure was used, having its disadvantages (Sec. 7.1.2). Hence investigating the performance of superhomogenization in *3D* would be of interest, especially for the axial control rod interfaces.

---

## Acknowledgments

Of all people I would like to thank, first out is my main supervisor Henrik Nylén. Even though most of my time was spent in France, the communication through both mail and Skype was great!

To my supervisors in France, David Blanchet and Robert Jaqcmin. David who I worked closest with during the whole project, and from whom I learnt a great deal of fast reactors. Robert I would like to thank for his more than excellent input when it came to interesting views of the problems at hand, and the article writing with your exceptional scientific English skills.

A special thanks to all the previous and present colleagues at Chalmers, and especially Imre Pázsit and Hoai Nam Tran, who were involved in my project.

To all people at SPRC that helped me during this thesis, and I hope my work will come to good use for you in the future.

Vetenskapsrådet I would like to acknowledge for the full financial support of the project. Including the fact that these projects were the first state grants concerning nuclear energy in many years (keep it up!).

For the people whom I shared the lunches (including all the strange conversations), evenings, and leisure time with during the stay in France. Of course a shout out to my Swedish friends that visited me in France to lighten up some of my weekends.

Finally I would like to thank my family who supported me throughout this work, and of course to my new nephew Niclas, who I could not see much his first year on this earth since I had to be in France.



---

## BIBLIOGRAPHY

- [1] DOE. *CP-1 GOES CRITICAL*. [https://www.osti.gov/opennet/manhattan-project-history/Events/1942-1944\\_pu/cp-1\\_critical.htm](https://www.osti.gov/opennet/manhattan-project-history/Events/1942-1944_pu/cp-1_critical.htm). Accessed: 2016-07-12. 2016.
- [2] R. Michal. "Fifty years ago in December: Atomic Reactor EBR-I Produced First Electricity". In: *Nuclear News* (Nov. 2001), pp. 28–29.
- [3] OECD/NEA. *Technology Roadmap Update for Generation IV Nuclear Energy Systems*. Tech. rep. OECD/NEA, Jan. 2014.
- [4] C. Westfall. "Vision and reality: The EBR-II story". In: *Nuclear News* (Feb. 2004), pp. 25–32.
- [5] V. Pascal, G. Pruihère, M. Vanier, and B. Fontaine. "Interpretation of the Control Rod Withdrawal test in the Sodium-Cooled Fast Reactor Phénix." In: *Nucl. Sci. Eng* 175 (2013), pp. 109–123.
- [6] J. Gourdon, B. Mesnage, J. L. Voitellier, and M. Suescun. "An Overview of Superphénix Commissioning Tests". In: *Nucl. Sci. Eng* 106 (1990), pp. 1–10.
- [7] Yu. K. Buksha et al. "Operation Experience of the BN-600 Fast Reactor". In: *Nucl. Eng. Design*. 173 (1997), pp. 67–79.
- [8] I. Krivitski, M. Vorotyntsev, V. Physhin, and L. Korobeinikova. "Safety Analysis of Fast Reactor Core with Uranium-free Fuel for Actinide Transmutation". In: *Nucl. Sci. Eng*. 140 (2002), pp. 205–222.
- [9] U. Wehmann, H. Kinjo, and T. Kageyama. "Studies on Plutonium Burning in the Prototype Fast Breeder Reactor Monju". In: *Nucl. Sci. Eng*. 140 (2002), pp. 205–222.
- [10] B. Fontaine et al. "The French R&D on SFR core design and ASTRID project". In: *Proceedings of GLOBAL*. Makuhari, Japan, Dec. 2011.
- [11] J.L. Rowlands and C.R. Eaton. "The Spatial Averaging of Cross Sections for use in Transport Theory Calculations with and Application to Control Rod Fine Homogenisation". In: *Specialists meeting on homogenisation methods in reactor physics*. Lugano, Switzerland, 1978.
- [12] J. C. Gauthier et al. "Measurement and Predictions of Control Rod Worth". In: *Nucl. Sci. Eng* 106 (1990), pp. 18–29.

- [13] G. Choppin, J-O. Liljenzin, and J. Rydberg. *Radiochemistry and Nuclear Chemistry, Third Edition*. Butterworth-Heinemann, 2002.
- [14] SKB. *Our Method of Final Disposal*. <http://www.skb.com/future-projects/the-spent-fuel-repository/our-methodology/>. Accessed: 2015-01-20. 2015.
- [15] World Nuclear Association. *Nuclear Power in Finland*. <http://www.world-nuclear.org/info/Country-Profiles/Countries-A-F/Finland/>. Accessed: 2015-01-20. 2015.
- [16] OECD/NEA. *Actinide and Fission Product Partitioning and Transmutation, Status and Assessment Report*. Tech. rep. OECD/NEA, May 1999.
- [17] Chang. J. *Table of Nuclides, KAERI(Korea Atomic Energy Research Institute)*. <http://atom.kaeri.re.kr/>. Accessed: 2016-02-02. 2016.
- [18] A. Alembreti et al. "European Lead Fast Reactor-ELSY". In: *Nucl. Eng. Design* 241 (2011), pp. 3470–3480.
- [19] H. Abderrahim, P. Baeten, D. De Bruyn, and R. Fernandez. "MYRRAH - A Multi-Purpose Fast Spectrum Research Reactor". In: *Energy Conversion and Management* 63 (2012), pp. 4–10.
- [20] Z. Perkó et al. "Core neutronics characterization of the GFR2400 Gas Cooled Fast Reactor". In: *Prog. Nucl. Energy* 83 (2015), pp. 460–481.
- [21] A. E. Waltar and A. B. Reynolds. *Fast breeder reactors*. Pergamo Press, 1980.
- [22] F. Varaine et al. "Pre-Conceptual Design Study of ASTRID Core". In: *Proc. Int. Cong. on Advances in Nucl. Power Plants (ICAPP2012)*. Chicago, Illinois: American Nuclear Society, June 2012.
- [23] D. Blanchet and B. Fontaine. "Control Rod Depletion in Sodium-Cooled Fast Reactor: Models and Impact on Reactivity Control". In: *Nucl. Sci. Eng* 177 (2014), pp. 260–274.
- [24] J. L. Rowlands. "Physics of fast reactor control rods". In: *Prog. Nucl. Energy*. 16.3 (1985), pp. 287–321.
- [25] Ph. Dünner, H.-J. Heuvel, and M. Hörle. "Absorber materials for control rod systems of fast breeder reactors". In: *Journal of Nuclear Materials* 124 (1984), pp. 185–194.
- [26] K. Devan, A. Riyas, M. Alagan, and P. Mohanakrishnan. "A new physics design of control safety rods for prototype fast breeder reactor". In: *Ann. Nucl. Energy* 35 (2008), pp. 1484–1491.
- [27] B.T. Kelly, A.J. Brook, and B. Lambert. *Status of Fast Reactor Control Rod Development in the United Kingdom*. Tech. rep. IWGFR–48. International Atomic Energy Agency (IAEA), 1984, pp. 48–53.
- [28] S. Qvist and E. Greenspan. "An Autonomus Reactivity Control System for Improved Fast Reactor Safety". In: *Prog. Nucl. Energy* 77 (2014), pp. 32–47.

- 
- [29] M. Kambe and M. Uotani. "Design and Development of Fast Breeder Reactor Passive Reactivity Control Systems: LEM and LIM". In: *Nucl. Tech.* 122 (1997), pp. 179–195.
- [30] S. Beils et al. "Safety Objectives of SEPIA Systems for Sodium-cooled Fast Reactor". In: *ICAPP*. San Diego, CA, USA: American Nuclear Society, 2010.
- [31] M. Carta, G. Granget, and G. Palmiotti. "Control Rod Heterogeneity Effects in Liquid-Metal Fast Breeder Reactors: Method Developments and Experimental Validation". In: *Nucl. Sci. Eng* 100 (1988), pp. 269–276.
- [32] G. Bell and S. Glasstone. *Nuclear reactor theory*. Van Nostrand Reinhold Company, 1970.
- [33] C. Demazière. "Multi-physics modelling of nuclear reactors: current practices in a nutshell". In: *Int. Jour. of Nucl. Sci. and Tech* 7.4 (2013), pp. 288–318.
- [34] C. Demazière. *Modelling of Nuclear Reactors*. Chalmers University of Technology, 2010.
- [35] R. Sanchez. "Assembly Homogenization Techniques for Core Calculations". In: *Prog. Nucl. Energy* 51 (2009), pp. 14–31.
- [36] K. S. Smith. "Assembly Homogenization Techniques for Light Water Reactor Analysis". In: *Prog. Nucl. Energy* 17.3 (1986), pp. 303–335.
- [37] D. C. Wade and R. G. Bucher. "Conservation of the Adjoint Neutron Spectrum by use of Bilinear-Weighted Cross Sections and its Effect on Fast Reactor Calculations". In: *Nucl. Sci. Eng* 64 (1977), pp. 517–538.
- [38] A. Hébert and G. Mathonnière. "Development of a Third-Generation Super-Homogenizations Method for the Homogenization of a Pressurized Water Reactor Assembly". In: *Nucl. Sci. Eng* 155 (1993), pp. 129–141.
- [39] E. Nikitin, E. Fridman, and K. Mikityuk. "On the use of the SPH Method in Nodal Diffusion Analyzes of SFR Cores". In: *Ann. of Nucl. Energy* 85 (2015), pp. 544–551.
- [40] E. Sartori. *Standard Energy Group Structures of Cross Section Libraries for Reactor Shielding, Reactor Cell and Fusion Neutronics Applications: VITAMIN-J, ECCO-33, ECCO-2000 and XMAS, JEF/DOC-315, Revision 3, NEA Data Bank*. Gif-sur-Yvette Cedex, France, Dec. 1990.
- [41] G. Rimpault et al. "The ERANOS Data and Code System for Fast Reactor Neutronic Analyses". In: *Proceedings of PHYSOR*. Seoul, South Korea, Oct. 2002.
- [42] G. Rimpault. "Algorithmic Features of the ECCO Cell Code for Treating Heterogeneous Fast Reactor Assemblies". In: *Proc. Int. Topical Meeting on Reactor Physics and Computations*. Portland, USA, May 1995.
- [43] G. Palmiotti, J.-M. Rieunier, C. Gho, and M. Salvatores. "Optimized Two-Dimensional  $S_N$  Transport (BISTRO)". In: *Nucl. Sci. Eng* 104 (1990), pp. 26–33.

- [44] C. B. Carrico, E. E. Lewis, and G. Palmiotti. "Three-Dimensional Variational Nodal Transport Methods for Cartesian, Triangular, and Hexagonal Criticality Calculations". In: *Nucl. Sci. Eng* 111.2 (1992), pp. 168–179.
- [45] R. Le Tellier, C. Suteau, D. Fournier, and J.M. Ruggieri. "High-Order Discrete Ordinate Transport in Hexagonal Geometry: a new Capability in ERANOS". In: *21st International Conference on Transport Theory (ICTT-21)*. Torino, Italy, July 2009.
- [46] E. Brun et al. "Overview of TRIPOLI4 version 7 Continuous Energy Monte Carlo Code". In: *Proc. Int. Cong. on Advances in Nucl. Power Plants (ICAPP2011)*. Nice, France: ACM Press, May 2011.
- [47] B. E. Watt. "Energy Spectrum of Neutrons from Thermal Fission of  $U^{235}$ ". In: *Phys. Rev.* 87 (6 Sept. 1952), pp. 1037–1041.
- [48] P. Sciora et al. "Low Void Effect Core Design Applied on 2400 MWth SFR Reactor". In: *Proceedings of ICAPP*. Nice, France: ACM Press, May 2011.